1979

Molar heat capacity from 1 K to 60 K of triclinic sodium and lithium tungsten oxides and of d-hcp lanthanum

Pai-Hung Pan
Iowa State University

PAN, PAI-HUNG
MOLAR HEAT CAPACITY FROM 1 K TO 60 K OF TRICLINIC SODIUM AND LITHIUM TUNGSTEN OXIDES AND OF D-HCP LANTHANUM.

IOWA STATE UNIVERSITY, PH.D., 1979

Molar heat capacity from 1 K to 60 K of triclinic sodium and lithium tungsten oxides and of d-hcp lanthanum

by

Pai-Hung Pan

A Dissertation Submitted to the
Graduate Faculty in Partial Fulfillment of
The Requirements for the Degree of
DOCTOR OF PHILOSOPHY

Department: Physics
Major: Solid State Physics

Approved:

Signature was redacted for privacy.

In Charge of Major Work

Signature was redacted for privacy.

For the Major Department

Signature was redacted for privacy.

For the Graduate College

Iowa State University
Ames, Iowa

1979

TABLE OF CONTENTS

LIST OF FIGURES

LIST OF TABLES

I. INTRODUCTION

A. Triclinic Sodium and Lithium Tungsten Oxide Crystals

The tungsten bronzes are a series of nonstoichiometric compounds with the general formula M_xWO_3, where M is usually a metallic element and $0 < X < 1$. In all cases, the structure is composed of linked WO_6 octahedra with M atoms filling the interstitial sites. As the x-value increases for a given M, it is generally found that the symmetry of the structure also increases. This empirical feature for some bronzes is illustrated in Fig. 1. For alkali tungsten bronze, Magneli (1) has shown that the hexagonal structure is composed of three- and six-member rings of the corner bonded WO_6 octahedra with M atoms located in the hexagonal channel along the c-axis. The tetragonal-I structure consists of similarly bonded five-member rings. In the cubic structure, the WO_6 octahedra form rectangular channels occupied by the M atoms.

Sodium tungsten bronze crystals Na_xWO_3 have been grown successfully in this laboratory by fused salt electrolysis of the Na_2WO_4-WO_3 molten mixture. The phase and the x-value of a grown crystal depend on the growth condition, the mole % of WO_3, and the growth temperature. Details of the phase diagram for the growth of Na_xWO_3 as reported by Shanks (2) are shown in Fig. 2.

During the process of growing the tetragonal sodium tungsten bronze single crystals with the x-value near 0.3, a number of crystals with triclinic symmetry were obtained. After careful investigation, Shanks (2) found that these triclinic single crystals grow at or just

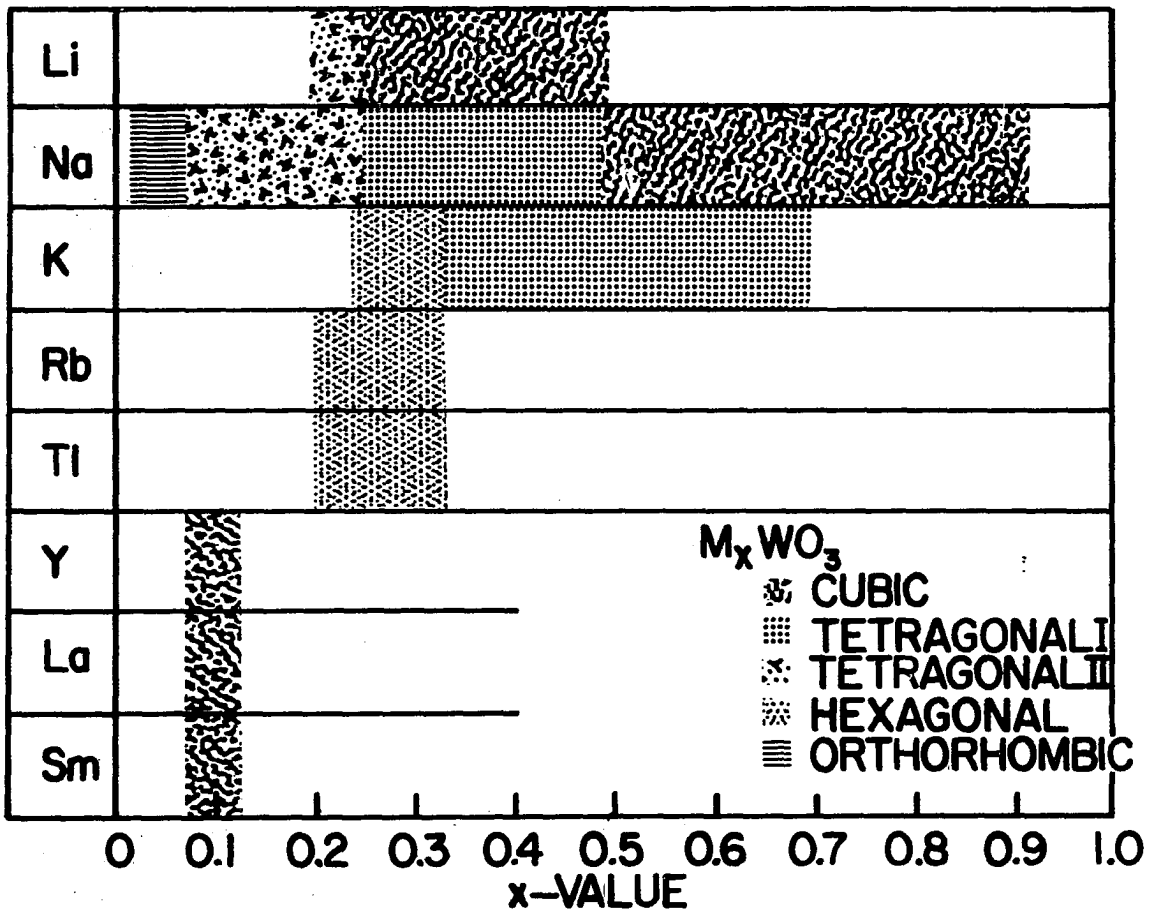

Figure 1. Dependence of crystal structure on x-value for several tungsten bronzes. The crystal symmetry increases with increasing x-value. Tetragonal I and hexagonal bronzes are superconductors; tetragonal II and orthorhombic bronzes are semiconductors. (Chart was prepared by H. R. Shanks.)

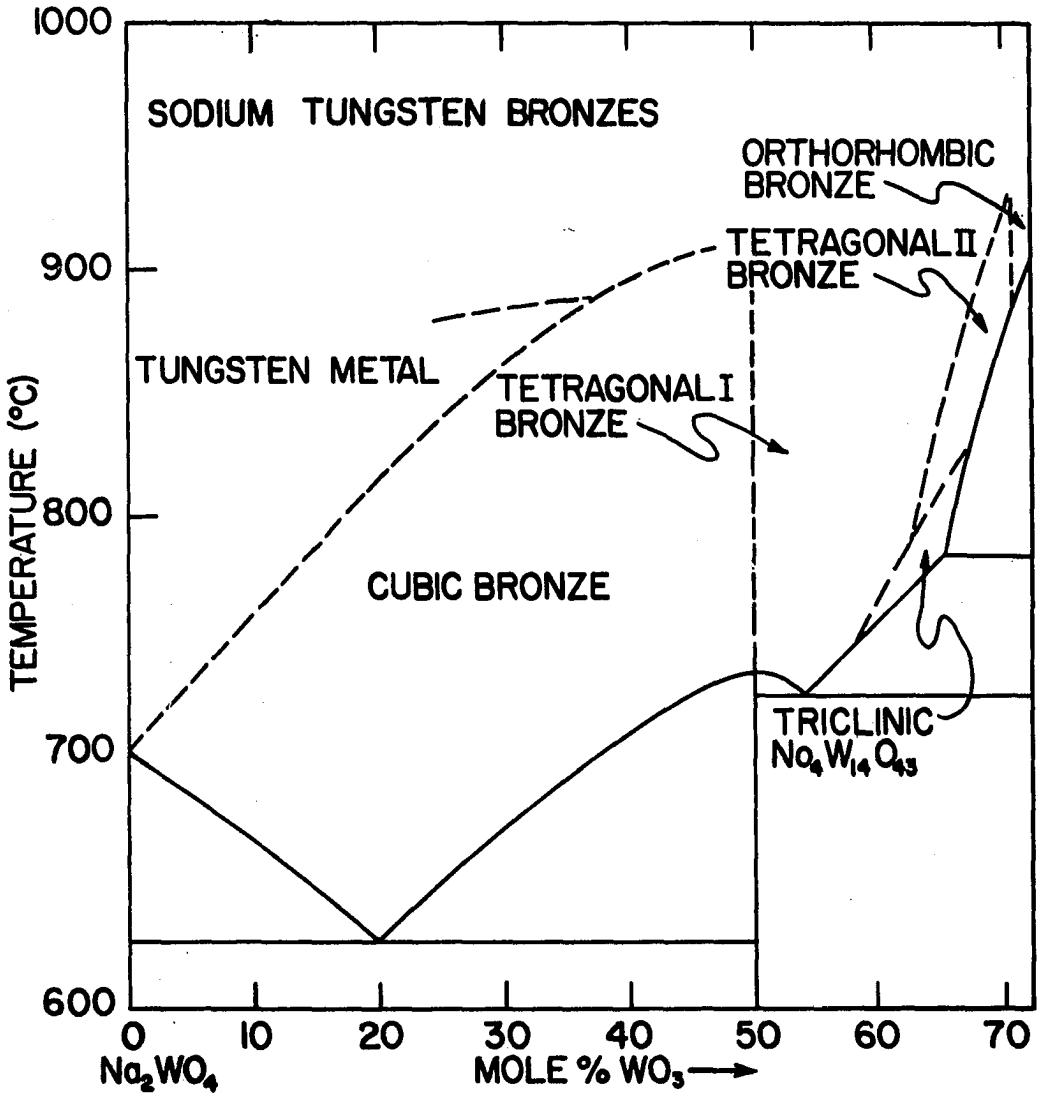

Figure 2. The phases of sodium tungsten bronze obtained by electrolysis as a function of melt composition. The liquidus curve is taken from the Na_2WO_4-WO_3 phase diagram of Mellor. (After H. R. Shanks, (Ref. 2))

above the melting point of the molten mixture of Na_2WO_4 and WO_3. Based on a single crystal x-ray diffraction study, Franzen et al. (3) suggested that the structure of the triclinic single crystal is composed of four layers having roughly the layer structure found in hexagonal bronzes and a fifth layer linking those four layers. The suggested tungsten layers are shown in Fig. 3. In all layers the tungsten atoms are linked by distorted octahedra of oxygen atoms except in the third layer where they are linked by a trigonal-bipyramid of oxygen atoms. The sodium atoms are thought to be in the unaligned hexagonal holes in the other layers.

Triclinic single crystal of $Li_{0.33}WO_3$ were also grown by fused salt electrolysis of the Li_2WO_4-WO_3 melts. The growth condition for the $Li_{0.33}WO_3$ sample is nearly the same as that for the $Na_{0.33}WO_3$ sample and the structure of $Li_{0.33}WO_3$ is isomorphic with that of $Na_{0.33}WO_3$.

A number of heat capacity studies for various tungsten bronzes have been reported previously. Vest et al. (4) measured several cubic Na_xWO_3 from 1 K to 4.2 K, and found the γ-value increased with increasing x-value. Gerstein et al. (5) reported the specific heat of cubic $Na_{0.69}WO_3$ from 1.5 K to 300 K and found a minimum of the Debye temperature at about 27 K. Kienzle et al. (6) have measured C_p of five Rb_xWO_3 from 1 K to 16 K, and observed that the T_c is not sensitive to the x-value ($0.27 < x < 3.2$). In the above measurements, no heat capacities with Einstein contribution were reported. King et al. (7) have reported the heat capacity of hexagonal Rb_xWO_3 with an x-value near 0.33 from 1.5 K to 16 K and found an excess heat capacity which could be attributed

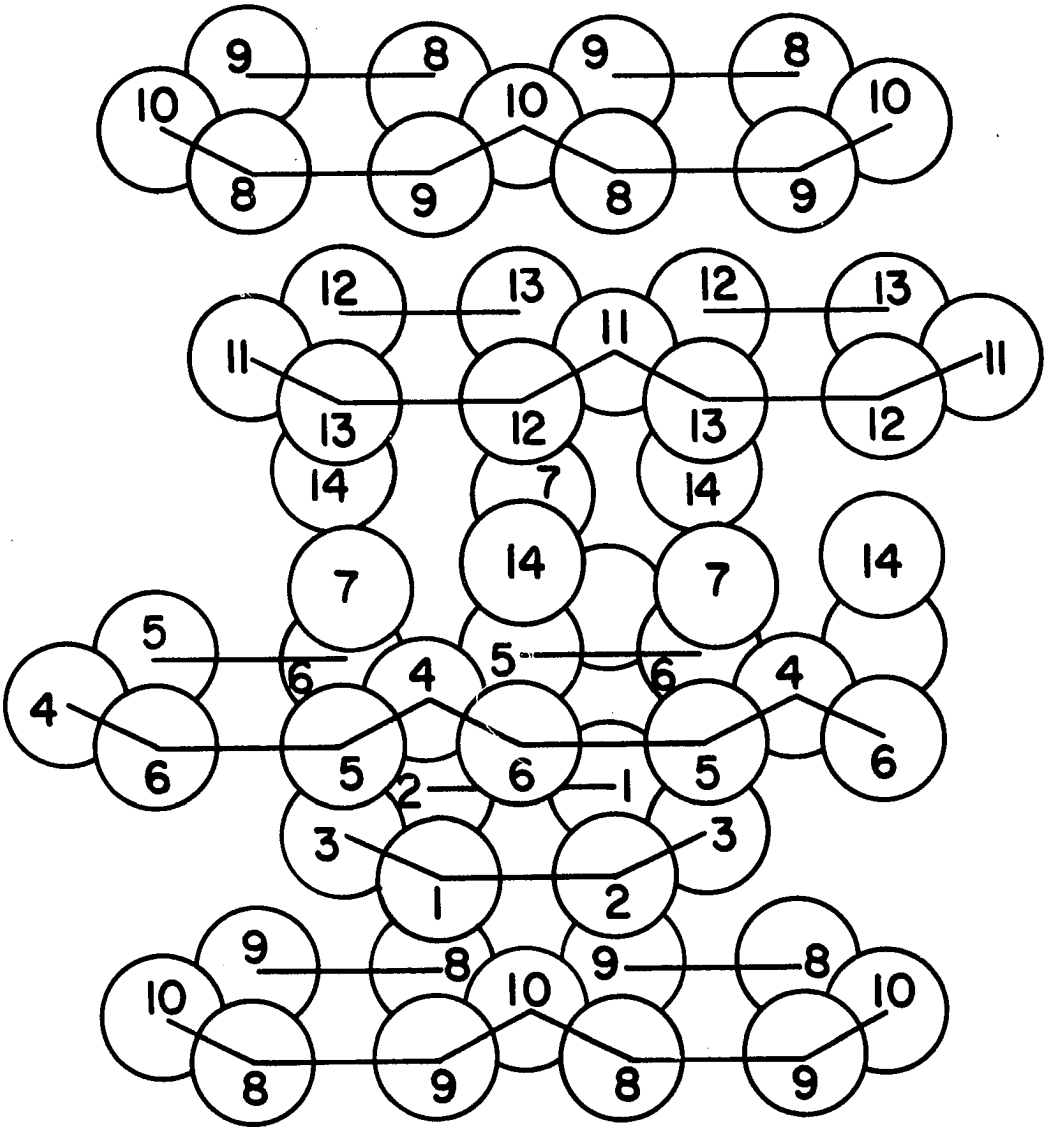

Figure 3. The fifth, first, second, third, fourth and fifth tungsten layers for the triclinic sodium tungsten oxide crystal

to an Einstein mode. Bevolo et al. (8) measured four hexagonal bronzes (K_xWO_3, Rb_xWO_3, Cs_xWO_3, and Tl_xWO_3), and observed an excess heat capacity present in all four bronzes. This excess heat capacity could also be attributed to an Einstein mode. This similar result obtained by King et al. (7) and by Bevolo et al. (8) by different methods suggested the presence of an Einstein-like excess heat capacity in the hexagonal symmetries.

The primary motivation of the work reported here is to study the possible existence of Einstein modes in crystals having the triclinic crystal structure and to compare them with the modes found in hexagonal symmetries. Bevolo et al. (8) have made point-ion estimates for the frequencies for the hexagonal case and found rather good agreement with the data. If possible modes in the triclinic crystals can also be predicted in this way, it will add significantly to the credibility of these calculations.

B. Lanthanum

Lanthanum, which is the first element of the lanthanide series, can exist in both hexagonal closed-packed (d-hcp) phase and face-centered cubic (fcc) phase, and as the metal occurs, it contains both crystal-structure phases. Rather special preparation techniques are required to produce pure phase samples because the free energy difference between these phases is rather small. Early studies (9) indicated that there might be two separate superconducting transitions for the samples measured, one for each phase. Later a thorough study of the crystal

structure and the superconductivity of La by Ziegler et al. (10) showed that the d-hcp and fcc La are indeed both superconducting but with different transition temperatures.

In the early studies of superconductivity in La, there has been a large disparity of results primarily because it is so difficult to obtain high purity single phase material. Using the magnetic susceptibility method, the transition temperature of La was reported to be 4.7 by Mendelssohn and Daunt (9), 4.85 K and 4.44 K by Ziegler and Horn (11) and 5.0 K for d-hcp La and 5.95 K for fcc La by Anderson et al. (12). By the electrical resistivity measurement, James et al. (13) found the transition temperature T_c ranging from 5.5 K to 6.0 K, and Legvold et al. (14) reported that the T_c values of four high purity d-hcp La metal with more than 98% pure d-hcp phase were from 5.15 K to 5.32 K. This is an unusually large variation of T_c values and clearly indicates the need for improved sample preparation.

In addition to these large differences in T_c, unusual behavior also was found in other properties. From the far-infrared absorption measurement reported by Leslie et al. (15), the energy gap $2\Delta(0)$ for a superconducting fcc La metal was found to be 2.85 $k_B T_c$, a value far below theoretical predictions. The tunneling results reported by Edelstein and Toxen (16) and Hauser (17) gave values of $2\Delta(0)/k_B T_c$ ranging from 1.65 to 3.2. These values of energy gap are lower than the BCS value ($2\Delta(0)/k_B T_c = 3.53$) and indeed lower than the value most superconductors ($3.2 < 2\Delta(0)/k_B T_c < 3.8$). It is fairly common to have $2\Delta(0)/k_B T_c > 3.53$ if strong coupling effects are present, but it is

unusual to have $2\Delta(0)/k_BT_c$ consistently much less than the BCS prediction. Anisotropy can depress $2\Delta(0)/k_BT_c$ by a few percent but there is no generally accepted theory which will give $2\Delta(0)/k_BT_c$ a factor of 2 less than BCS value. In view of this, there have been considerable skepticism about these early results. More recent data by Levinstein et al. (18) using point-contact tunning into bulk La suggested the value of $2\Delta(0)/k_BT_c$ ranging from 3.6 to 3.9 for the d-hcp La and 3.9 for the fcc La, these energy gap values are higher than the BCS prediction and consistent with the specific heat of Johnson and Finnemore (19).

Low-temperature heat capacity of lanthanum has been reported by Parkinson et al. (20), Berman et al. (21), Finnemore et al. (22), and Johnson and Finnemore (19). Parkinson et al. (20) measured the heat capacity of a La sample, which showed both the α and β phase lines on the x-ray analysis, from 2 K to 180 K and found a single superconducting transition at $T_c = 4.37$ K. Berman et al. (21), on the other hand, reported the specific heat of three La samples for $1.6 < T < 6.5$ K, and found two superconducting transitions for all samples, one associated with the d-hcp phase at T = 4.8 K, and another associated with the fcc phase at T = 5.9 K. They also found that $\gamma = 10$ mJ/mole-k^2 and $\theta_D = 142$ K for their purest sample. Finnemore et al. (22) have measured a La sample with nearly pure d-hcp phase from 1 K to 10 K and found that the transition temperature T_c is at 4.9 K and the jump in heat capacity at T_c is $\Delta C = 1.5\ \gamma\ T_c$, which is in good agreement with the BCS value ($\Delta C = 1.43\ \gamma\ T_c$). Johnson and Finnemore (19) have reported the specific heat from 1 K to 10 K for two La samples, one with 96%

of pure d-hcp phase, and another with 91% of pure fcc phase. They obtained γ_α = 9.4 mJ/mole-k^2, γ_β = 11.5 mJ/mole-k^2, $\theta_{D\alpha}$ = 152 K, $\theta_{D\beta}$ = 140 K, $T_{c\alpha}$ = 4.87 K, $T_{c\beta}$ = 6.00 K, $\Delta C_\alpha = 1.71\ \gamma_\alpha T_{c\alpha}$, $\Delta C_\beta = 1.73\ \gamma_\beta T_{c\beta}$, $2\Delta_\alpha(0) = 3.67\ k_B T_{c\alpha}$, and $2\Delta_\beta(0) = 3.69\ k_B T_{c\beta}$, where the subscripts α and β indicate the pure d-hcp and the pure fcc phase respectively. In addition, they found the data for both phases of La closely relate to the law of corresponding states and also agreed well with the prediction of BCS theory. Except for the result found by Parkinson et al. (20), which only had 30 data points from 2 K to 6 K, all measurements agree that there are two superconducting transitions for La metal with a mixture of the α and β phases. The disparities in T_c, $\Delta C/\gamma T_c$, etc. are also present in these heat capacity measurements.

In all of this earlier work, there was no serious attempt to determine whether La was type-I of type-II superconductor, because the purity was not high enough. Within the Ginzburg Landau theory, there are two distinct types of magnetic behavior for a superconductor depending on the so called Ginzburg Landau Kappa parameter which is approximately the ratio of the penetration depth λ to the coherence distance ξ. If $K \simeq \lambda/\xi < 1/\sqrt{2}$, the sample is said to be type-I and the super-normal phase transition is first order. For this case, the sample transforms directly from the Meissner state to the normal state at a field H_c. If $K > 1/\sqrt{2}$, the sample is said to be type-II and the sample goes from the Meissner state to the vortex state at a field H_{c1} and from vortex state to the normal state at a higher field H_{c2}. The super-normal transition at H_{c2} is second order. Both λ and ξ are controlled

by the electronic mean free path, so a sample can be made to change from type-I to type-II by altering the purity. As shown by Goodman, the expression for K is $K = K_o + K_\ell$, where $K_o = 0.96\lambda_o/\xi_o$ is an intrinsic term and $K_\ell = 7.53 \times 10^3 \gamma^{\frac{1}{2}} \rho_o$ depends on the electronic mean free path. In the limit as the metal becomes more pure, $\rho_o \to 0$ and the K goes to the intrinsic value. By measuring H_{c2} and H_{c1}, one can determine K and hence the ratio of λ and ξ.

Recently much higher purity La has become available by using the solid state electrotransport method (23). In this purifying process, a La rod was heated by passing a high density D.C. electrical current through the metal rod, which caused impurities to migrate either with or against the flow of the electrons. After purification by the electrotransport method, the gas impurities in the sample are found to be reduced more significantly than the other impurities. Normally, the center section is very pure and has a resistivity ratio of the order of 100 compared with a resistivity ratio of the order of 10 in the starting metal.

The purpose of the work reported here is to study the low-temperature heat capacity of high purity electrotransported La sample with a high percent of d-hcp phase and to determine the purity dependence of fundamental parameters such as γ and θ_D. Because the heat capacity at low temperature supplies many important parameters about a solid in the normal and superconducting state, this study will provide the fundamental parameters needed to compare the band structure calculations of T_c. In addition, an extensive series of measurements of C_p in a magnetic field

provide a clear means to determine whether the d-hcp La is an intrinsic type-II superconductor.

II. THEORY

A. Normal State

The low temperature heat capacity of a metal consists of electronic and lattice terms. The electronic heat capacity, which is contributed by the conduction electrons and can be derived from the free-electron theory, is linear in temperature. This is a very general calculation and applies for all metals for which the density of states N(E) does not change appreciably for an energy range of several $k_B T$ near the Fermi energy. For the lattice specific heat, the interpretation of the data is not quite as straightforward. The phonon density of states frequently has an energy dependence which is then reflected in the lattice heat capacity. Two models, Einstein's and Debye's are, commonly used to describe the lattice heat capacity. Under the assumptions made by the Einstein model, the phonon density of states $g(\nu)$ is a δ-function, i.e., $g(\nu) = N\delta(\nu - \nu_E)$ and the phonon dispersion relation ω vs. k is a constant independent of the wave vector k. For the Debye model the phonon density spectrum $g(\nu)$ is proportional to ν^2 and the dispersion curve in the ω-k plane has a constant group velocity. In the high-temperature limit, the results predicted by both models approach the Dulong and Petit value 3SR. At sufficiently low temperature, the Debye model predicts a term cubic in temperature while the Einstein model predicts a term exponential in temperature.

1. Electronic heat capacity

From quantum statistics, the total internal energy of a Fermi electron system is given by

$$\bar{U} = \int_0^\infty E\, D(E) f(E) dE$$

where

$$D(E) = \left(\frac{1}{2\pi^2} \right) \left(\frac{2m}{\hbar} \right)^{3/2} E^{1/2}$$

is the density of states of the electron gas at energy E,

$$f(E) = \frac{1}{[1 + \exp((E - E_F(T))/k_B T)]}$$

is the Fermi-Dirac distribution function and $E_F(T)$ is the Fermi energy at temperature T. Using Taylor's expansion, it can be shown that

$$\bar{U} = \frac{3}{5} E_F(0) \left[1 + \frac{5\pi^2}{12} \left(\frac{k_B T}{E_F(0)} \right)^2 + \ldots \right]$$

and

$$E_F(0) = \frac{\pi^2}{2m} (3\pi^2 N)^{2/3} \quad .$$

As $k_B T/E_F(0) << 1$, the heat capacity is given by

$$C \equiv \frac{\partial \bar{U}}{\partial T} = \left(\frac{\pi^2}{2} \right) \left(\frac{N k_B^2 T}{E_F(0)} \right) \quad .$$

Multiplication of this term by the molar volume, $V = \frac{ZR}{k_B n}$ yields the

molar electronic heat capacity

$$C_E = \left[\frac{\pi^2}{3n} ZR\, k_B D(E_F(0)) \right] T$$
$$= \gamma T \qquad (2.1)$$

where n is the electron density, Z is the number of conduction electrons per formula weight and $D(E_F(0)) = \frac{3n}{2E_F(0)}$ is the density of states at the Fermi energy at absolute zero. For typical metals, say, copper and sodium, the experimental γ values are 0.7 and 1.35 respectively, and the calculated γ values from Equation (2.1) are Cu = 0.54 and Na = 1.1, where the γ values are in units of $\frac{mJ}{mole - k^2}$. It is obvious that the free-electron model is oversimplified but gives a γ value of the right order of magnitude.

2. Einstein model of lattice heat capacity

According to quantum theory, the energy of an oscillator with frequency ν is given by $E_n = nh\nu$. In thermal equilibrium at temperature T, the average energy of an oscillator is

$$E_n = \frac{\sum_n E_n \exp(-E_n/k_B T)}{\sum_n \exp(-E_n/k_B T)}$$
$$= \frac{h\nu}{\exp(h\nu/k_B T) - 1} \qquad (2.2)$$

By assuming all atoms vibrate independently of one another with the same frequency ν_E, Gopal (24) shows that the molar lattice heat capacity is

$$C_E = \left(\frac{3}{4} R\right)(S)\left(\frac{T_E}{T}\right)^2 \operatorname{csch}^2\left(\frac{T_E}{2T}\right) \qquad (2.3)$$

where $T_E \equiv \frac{h\nu_E}{k_B}$ is called the Einstein temperature and S is the number of atoms per formula weight. At very high temperatures, this equation becomes

$$C_E = 3SR \qquad \text{as } T >> T_E$$

and at very low temperatures, this equation becomes

$$C_E = 3SR\left(\frac{T_E}{T}\right)^2 \exp\left(-\frac{T_E}{T}\right) \quad . \quad \text{as } T << T_E$$

3. Debye model of lattice heat capacity

Because at low temperatrue only the low frequency modes of lattice vibration will be appreciably excited in the crystal and the wavelength of the low frequency oscillation is much longer than the atomic dimension, Debye (25) used the idea of the propagation of acoustic waves in an elastic continuous medium to treat the phonons in crystal. Within the Debye model, it is assumed that the frequency of vibration is distributed from 0 to a maximum value ν_0, and the elastic continuous frequency distribution function is

$$g(\nu) = \frac{3\nu^2}{\nu_0^3} \qquad \text{for } \nu \leq \nu_0$$

$$= 0 \quad . \qquad \text{for } \nu > \nu_0$$

The total energy per mole can be written as

$$\bar{U} = (3rN) \int_0^{\nu_0} \bar{E}\, g(\nu) d\nu$$

where (3rN) is the total number of modes per mole and $\bar{E}$ is the average energy from Equation (2.2). It can then be shown that the total energy is

$$\bar{U} = \frac{3rN\, k_B\, \theta_D}{8} + \frac{9rN\, k_B T^4}{\theta_D^3} \int_0^{\theta_D/T} \frac{y^3}{e^y - 1}\, dy$$

and the molar lattice heat capacity is

$$C \equiv \frac{\partial \bar{U}}{\partial T} = 9rN\, k_B \left[\frac{4\pi^2}{\theta_D^3} \int_0^{\theta_D/T} \frac{y^3}{e^y - 1}\, dy - \frac{\theta_D/T}{e^{\theta_D/T} - 1} \right]$$

where $\theta_D \equiv \frac{h\nu_0}{k_B}$ is called the Debye temperature, N is the total number of atoms, r is the number of atoms per formula weight contributing to the Debye model and $y \equiv \frac{h\nu}{k_B T}$.

At high temperature, θ_D/T and y are very small. Therefore the integral approaches y^2, so that

$$C_D = 3rR \left[1 - \frac{1}{20} \left(\frac{\theta_D}{T} \right)^2 + \ldots \right] .$$

At very low temperature, the upper limit of the integration can be taken as infinite. Thus,

$$C_D = \frac{1944r}{\theta_D^3} T^3 \quad \left(\text{in units of } \frac{J}{\text{mole} - k}\right)$$

$$= \beta T^3 \quad . \tag{2.4}$$

B. Superconducting State

Bardeen, Copper and Schrieffer (BCS) (26) have shown that the electron-phonon interaction in a metal can result in a net attractive interaction between electrons and this interaction leads to superconductivity and a temperature dependent energy gap $2\Delta(T)$ in the excitation spectrum of the electrons. From BCS theory, the energy gap at $T = 0$ is $2\Delta(0) = 3.53\ k_B T_c$ and the transition temperature T_c is given by

$$T_c = 1.14\ \theta_D \exp(-1/N(0)V_p) \tag{2.5}$$

where θ_D is the Debye temperature, V_p is the constant net attractive interaction and $N(0)$ is the density of state at the Fermi surface. This equation shows that the transition temperature is controlled by θ_D, $N(0)$ and V_p. Because the values of T_c, θ_D and $N(0)$ can be determined from the specific heat data, the strength of the fundamental interaction causing superconducting, V_p can be obtained from Equation (2.5).

In general, the heat capacity can be separated into an electronic contribution C_e and a lattice contribution C_g because they are nearly independent of each other. Thus, the heat capacity in the superconducting state and normal state can be written as

$$C_s = C_{es} + C_{gs}$$

$$C_N = C_{eN} + C_{gN}$$

where e and g denote electric and lattice, and N and s denote normal and superconducting. There is an extensive evidence that the lattice properties do not change between superconducting and normal state (27,28), and it is reasonable to assume that C_{gs} is equal to C_{gN}, the lattice heat capacity in normal state. It also has been shown by BCS that the jump in specific heat at T_c is given by

$$\frac{C_{es} - \gamma T_c}{\gamma T_c} = 1.43 \tag{2.6}$$

and at lower temperature an exponential behavior occurs,

$$C_{es} \approx a\, e^{-b/k_B T} \quad . \qquad \text{as } T << T_c \tag{2.7}$$

Here γ is the coefficient of the electronic heat capacity in the normal state, k_B is the Boltzman constant, a is a constant and b is another constant with a value near $\Delta(0)$, the energy gap parameter.

There are two types of superconductors, type-I and type-II, depending on the relative magnitude of two characteristic lengths, the penetration depth of magnetic field λ and the coherence length ξ. In terms of the Ginzburg-Landau parameter $K \equiv \frac{\lambda}{\xi}$, it is found that the separation point is $K = \frac{1}{\sqrt{2}}$, and for $K < \frac{1}{\sqrt{2}}$ one finds type-I behavior and for $K > \frac{1}{\sqrt{2}}$ one finds type-II behavior. These two qualitatively different types of response to a magnetic field are governed by the superconducting-normal metal surface energy. A type-I superconductor has a positive surface energy but a type-II superconductor has a negative surface energy.

The magnetization and the temperature dependent critical field of an ideal type-I superconductor are shown in Fig. 4. The Meissner effect, which is the name given to the expulsion of the magnetic flux from a substance at its transition from the normal state to the superconducting state, implies that the phase transition is reversible. We may therefore apply thermodynamic argument to a superconductor, using temperature and applied magnetic field as thermodynamic variables. With an applied magnetic field H, a substance in the superconducting state acquires a magnetization M and changes its Gibb's free energy by an amount

$$\Delta G \equiv G_s(H, T) - G_s(0, T) = -V \int_0^H M dH$$

where $G_s(H, T)$ is the Gibb's free energy of the superconducting state at temperature T, H is the applied magnetic field and V is the volume of the substance. When the magnetic field is applied along the axis of a long thin cylinder, the magnetization M is equal to $-H/4\pi$. Then, the change in the Gibb's free energy is given by

$$\Delta G = G_s(H, T) - G_s(0, T) = \frac{VH^2}{4\pi} \quad . \tag{2.8}$$

In the normal state, the substance is virtually nonmagnetic and acquires negligible magnetization in an applied magnetic field, i.e., $G_N(H, T) = G_N(0, T)$. If we consider a point on the phase transition curve, then $G_s(H_c, T) = G_N(H_c, T)$ and Equation (2.8) reduces to

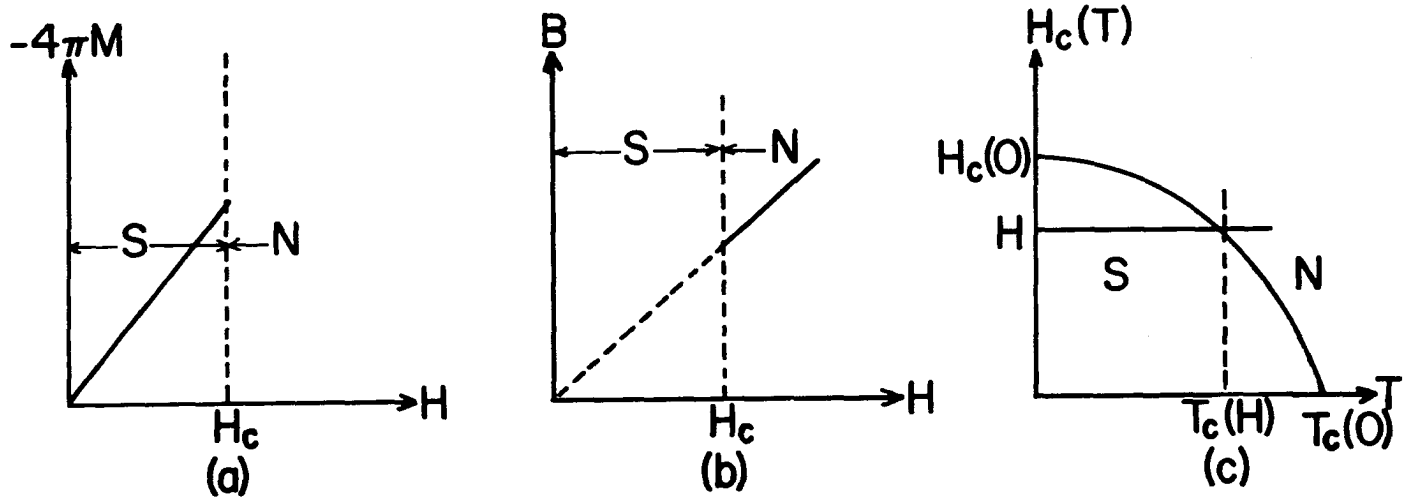

Figure 4. The magnetic properties of a type-I superconductor, where N and S indicate the normal and the superconducting state respectively.
(a) The magnetization M vs. the applied magnetic field H.
(b) The magnetic inductance as a function of the applied magnetic field H.
(c) The dependence of the critical field $H_c(T)$ on temperature

$$G_N(0, T) - G_s(0, T) = \frac{VH_c^2}{8\pi} \quad .$$

Therefore, the entropy difference

$$\Delta S \equiv S_N - S_s \equiv -\left(\frac{\partial G_N}{\partial T}\right) + \left(\frac{\partial G_N}{\partial T}\right)$$

is given by

$$\Delta S = \frac{-VH_c}{8\pi}\left(\frac{\partial H_c}{\partial T}\right)$$

and the heat capacity change

$$\Delta C \equiv C_N - C_s \equiv T\frac{\partial S_N}{\partial T} - T\frac{\partial S_s}{\partial T}$$

is given by

$$\Delta C = \frac{-VT_c}{4\pi}\left[\left(\frac{\partial H_c}{\partial T}\right)^2 + H_c\left(\frac{\partial^2 H_c}{\partial T^2}\right)\right] \quad . \tag{2.9}$$

From Equation (2.9), we know the phase transition at T_c is a first order transition with latent heat

$$L \equiv T\Delta S = \left(\frac{-VT_cH_c}{4\pi}\right)\left(\frac{\partial H_c}{\partial T}\right)$$

as $H \neq 0$, and is second order at $H = 0$. The heat capacity of a typical type-I superconductor as a function of temperature is shown in Fig. 6(a).

The magnetic properties of an ideal type-II superconductor is shown in Fig. 5. In a type-II superconductor there exists a mixed state

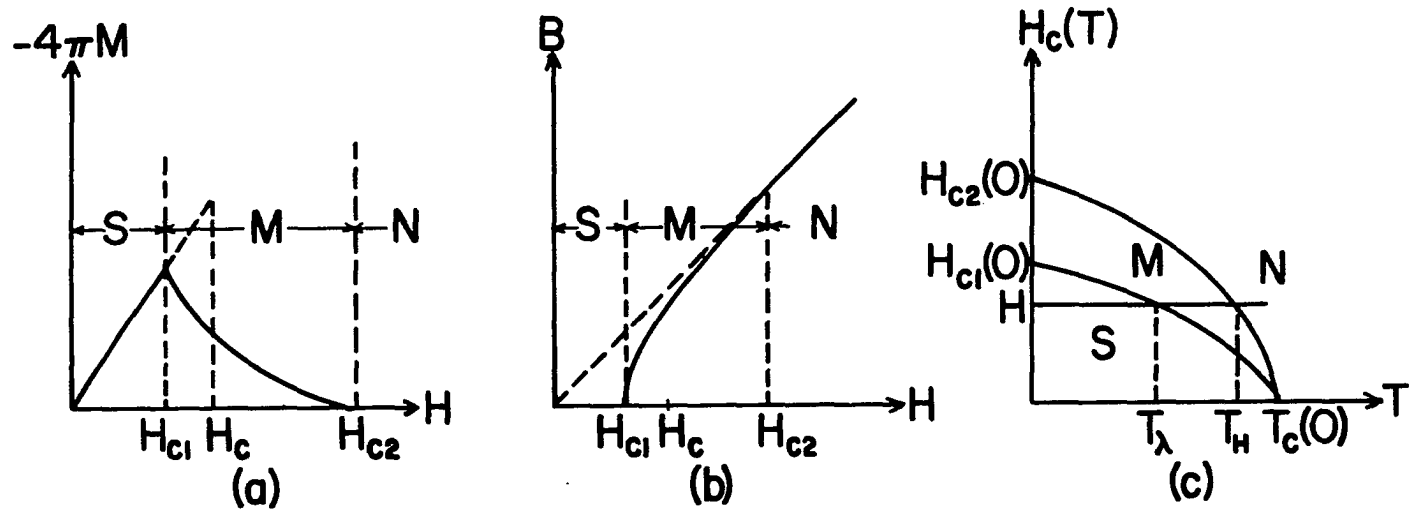

Figure 5. The magnetic properties of a type-II superconductor, where N, M, and S indicate the normal, the mixed and the superconducting state respectively.
(a) The magnetization M vs. the applied magnetic field H, as $H \to H_c^+$, the slope $\to \infty$.
(b) The magnetic inductance B as a function of an applied magnetic field H, as $H \to H_c^+$, the slope $\to \infty$.
(c) The dependence of the critical field $H_c(T)$ on temperature.

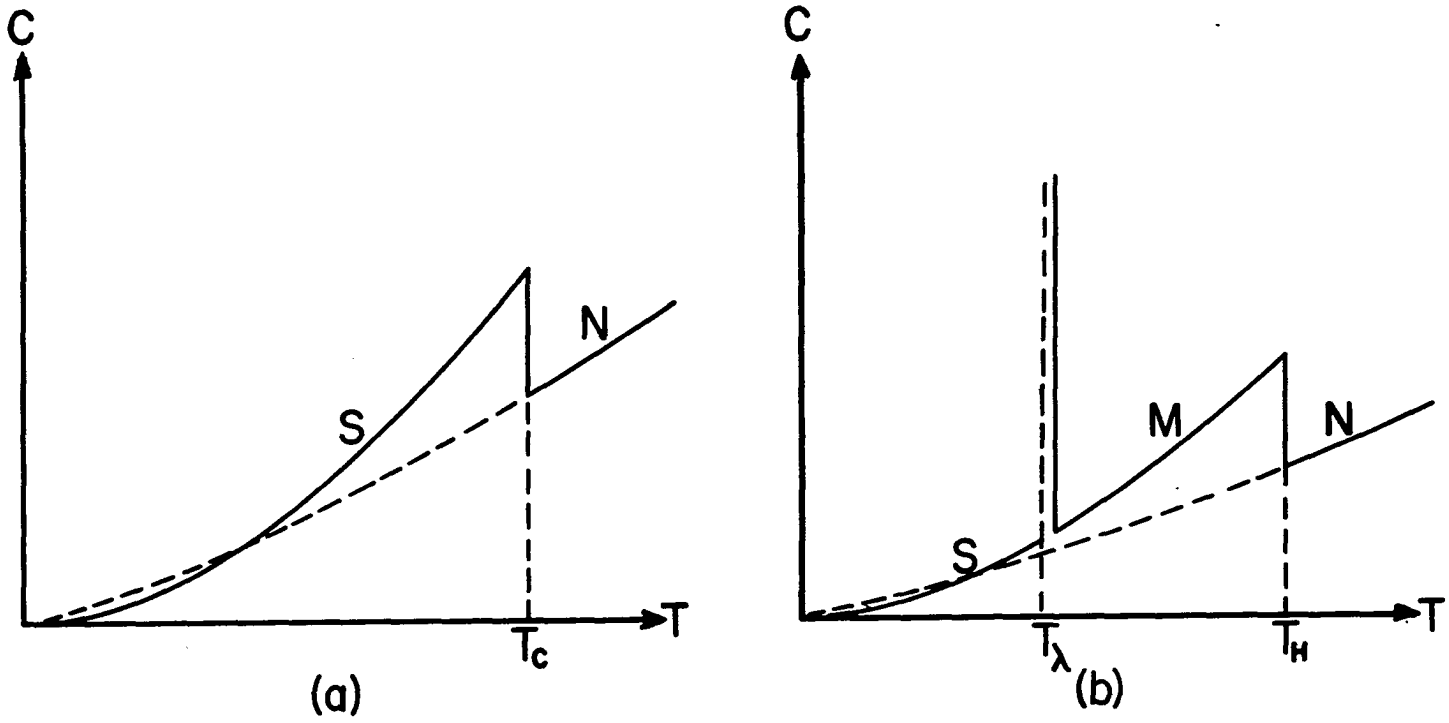

Figure 6. The heat capacity of a superconductor vs. temperature with an applied magnetic field H, where N, M, and S indicate the normal, mixed and superconducting state respectively.
(a) For a type-I superconductor ($H < H_c(0)$).
(b) For a type-II superconductor ($H < H_c(0)$)

region, which is a mixture of superconducting and normal states with quantized flux lines (called vortices) penetrating the specimen. With an applied magnetic field $H(H < H_{c1}(0))$, Fig. 5(c) shows that the substance will go through two phase transitions, normal $\leftrightarrow$ mixed and mixed $\leftrightarrow$ superconducting at $T = T_H$ and $T = T_\lambda$ respectively.

When one considers $H = H^*(T)$ in the H-T plane separating two phase i and j, and let the entropy be continuous in crossing the curve, de Gennes (29) has shown that

$$C_i - C_j = \left(\frac{T}{4\pi}\right)\left(\frac{dH^*(T)}{dT}\right)^2\left[\left(\frac{\partial B_i}{\partial H}\right)_T - \left(\frac{\partial B_j}{\partial H}\right)_T\right]$$

where C is the heat capacity, B is the magnetic inductance and the subscripts i, j indicate the two phase. As $|H - H_{c2}| << H_{c2}$ Abrikosov (30) has shown that the magnetic inductance of the mixed state is given by

$$B_M = H - \frac{K - H}{(2K^2 - 1)\beta_A} \quad .$$

Therefore,

$$\frac{\partial B_M}{\partial H} - \frac{\partial B_N}{\partial H} = [(2K^2 - 1)\beta_A]^{-1}$$

and the discontinuity in the heat capacity is

$$\Delta C_{MN} \equiv C_M - C_N = \frac{T}{4\pi}\left(\frac{dH_{c2}}{dT}\right)^2 [(2K - 1)\beta_A]^{-1} > 0$$

where K is Ginzburg-Landau parameter and β_A is a geometric constant

independent of K and H. This positive second order heat capacity jump at $T = T_H$ is shown in Fig. 6(b).

Let us consider the $H = H_{c1}(T)$ phase transition curve. As $0 < H - H_{c1} << H_{c1}$, the calculation of the magnetization curve in the mixed state given

$$\frac{\partial B_M}{\partial H} \approx \frac{4\phi_0}{\sqrt{3}\,\lambda^2(H - H_{c1})} \left\{ \ln\left[\frac{3\phi_0}{4\pi\lambda^2(H - H_{c1})} \right] \right\}^{-3} .$$

The above expression diverges as $H \to H_{c1}^{+}$. Therefore, the heat capacity at this mixed $\leftrightarrow$ superconducting phase transition will become singular as $T \to T_\lambda$. This λ-type phase transition was first noticed by Goodman (31), and this λ-type heat capacity jump at $T = T_\lambda$ is shown in Fig. 6(b).

III. EXPERIMENTAL

Heat capacity measurements were made by a heat-pulse method in a helium-4 cryostat of conventional design. The heat capacity was determined by the defining equation $C \equiv \frac{\Delta Q}{\Delta T}$ in a nearly thermal isolated system, where ΔQ is the total applied heat and ΔT is the temperature rise. The original apparatus was designed and constructed by W. Kienzle and was used extensively by Bevolo et al.

A. The Apparatus

A schematic diagram of the complete cryostat system is shown in Fig. 7. The outer cryostat, which consisted of an outer vacuum chamber and a liquid nitrogen dewar, was permanently mounted to the magnet system. The rest was called the inner cryostat and could be removed from the vacuum chamber. The nitrogen dewar and helium reservoir provided 77 K and 4 K environment respectively. The 4 K radiation shield was electrically isolated from the helium reservoir. Temperatures down to 0.9 K were achieved by closing the valve of the helium pot and pumping on the helium pot through an orifice. In order to minimize the conductive heat transfer to the sample chamber, the heat switch wire, all electrical leads and the pumping lines were thermally anchored to the nitrogen reservoir and helium reservoir. Copper disks were mounted horizontally in all pumping lines and thermally anchored to the nitrogen reservoir to serve as radiation shields. These shields reduced radiative heat transfer to the liquid helium reservoir. A homogeneous magnetic field across the tail of the cryostat was supplied

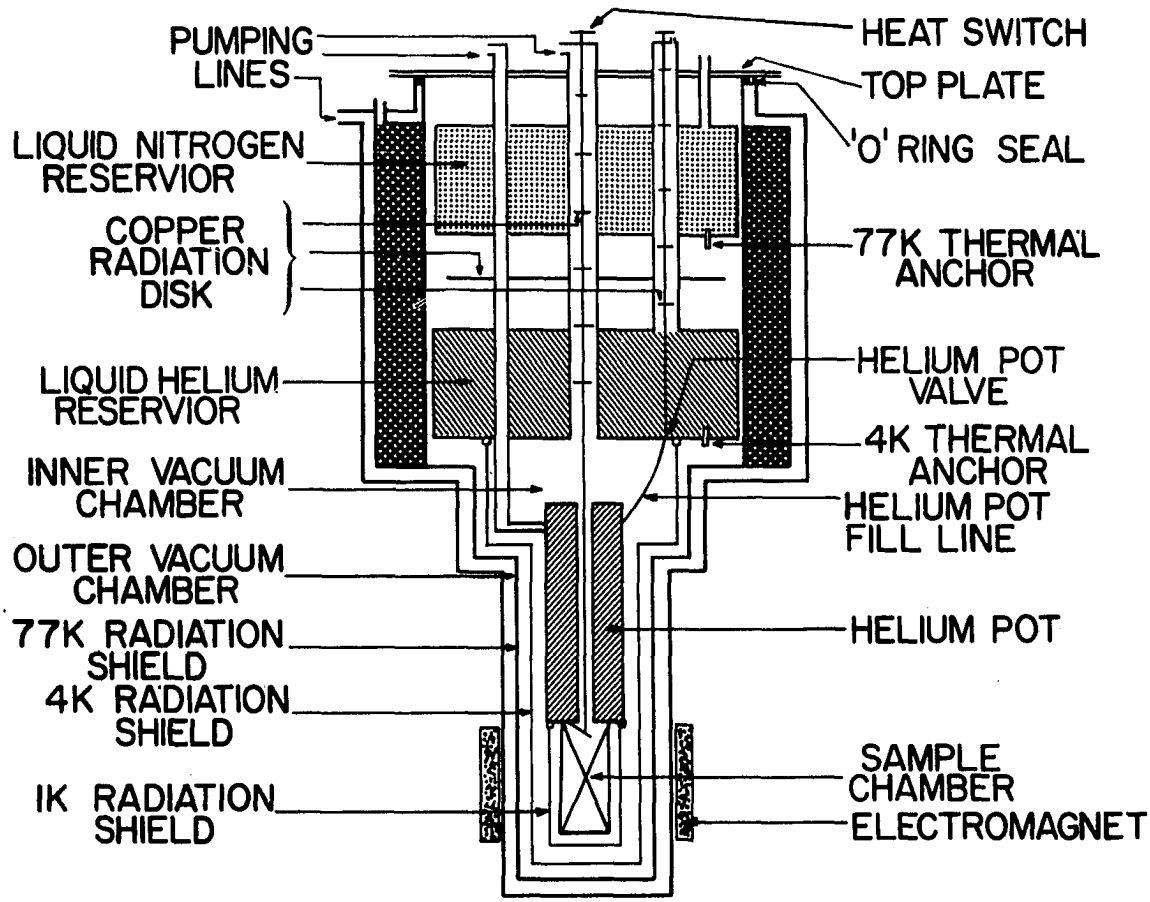

Figure 7. The complete cryostat for the heat capacity measurement

by a 12 inch Varian electromagnet. A hall-probe magnetometer was used to measure the applied magnetic field.

The diagram of the sample chamber is shown in Fig. 8. A mechanical heat switch was closed to cool down the sample and the addenda, which included the sample holder, heater, copper wire, Ge thermometer, fastening epoxy and 8 mg of Apiezon N-grease. To close the heat switch, the copper wire with one end silver soldered on the sample holder was clamped between a movable lower jaw and a copper post, which was soldered on the copper base of the helium pot. The sample holder was made of copper foil in the shape of a pan. A heater, which was made of 92% Pt + 8% W wire, was wound around the sample holder and was cemented to the holder with stycast epoxy. A Ge thermometer was also fastened with epoxy to a copper tab which was silver soldered on the bottom of the sample holder. In order to reduce the heat transfer to the sample holder, the floating sample holder which was fastened by 3 pairs of nylon threads was surrounded by 1 K, 4 K, and 77 K radiation shield and the pressure of the chamber was kept less than 10^{-6} Torr. In addition, all electrical leads were thermally anchored on a copper post soldered on the copper base of the helium pot and the 92% Pt + 8% W wire with low thermal conductivity and high electrical conductivity was used for electrical leads between the 1 K thermal anchor and the sample holder. These procedures of minimizing the heat transfer to the sample holder provide a nearly thermal isolated system for the heat capacity measurements.

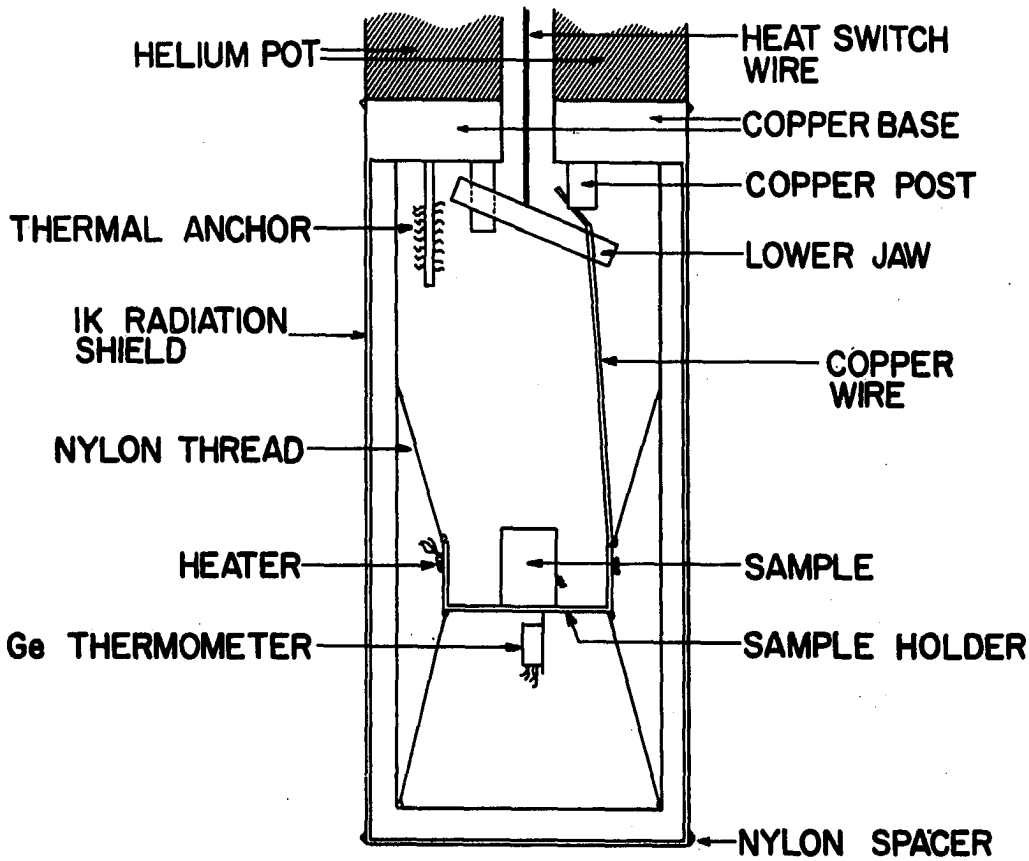

Figure 8. The sample chamber for the heat capacity measurement

The block diagram of the electrical circuit is shown in Fig. 9. The voltages across the 1000Ω standard resistance R_{SG} and the Ge thermometer were measured with a Leeds & Northrup No. 7556 potentiometer using a Keithley model 149 mill-microvoltmeter as a null detector. The output of the Keithley voltmeter was displayed in the drift trace of the No. 1 pen of the Leeds & Northrup model 620 strip chart recorder. A Rubicon 'B' potentiometer with a Leeds & Northrup No. 9834-1 D.C. null detector was used to measure the voltage across the standard resistance R_{SH} (1000Ω or 100Ω) in the heater circuit. A dummy heater was adjusted to prevent surges of the heater current as the heater was turned on or off. When the heater was turned on or off, the Hewlett Packard model 521 CR electronic counter, which was connected to a 10 K Hz Fairchild type 781 time-mark generator, and the No. 2 pen of the strip chart recorder were turned on or off within 0.7 msec. The start and finish of the applied heat pulse were recorded as a jump in the trace of the No. 2 pen.

B. Thermometer

A germanium resistance thermometer, which was calibrated by C. A. Swenson, was used to measure the temperature. From 1.08 K to 60 K, the Ge thermometer was calibrated by comparison with another standard Ge thermometer which was calibrated against the paramagnetic salt temperature scale (32) from 1.08 K to 20 K and the NBS 1955 temperature scale from 20 K to 60 K. The calibration from 0.85 K to 1.33 K was done by placing a pure thorium single crystal in the calorimeter and determining the resistance of the Ge thermometer R(H) at the thorium transition

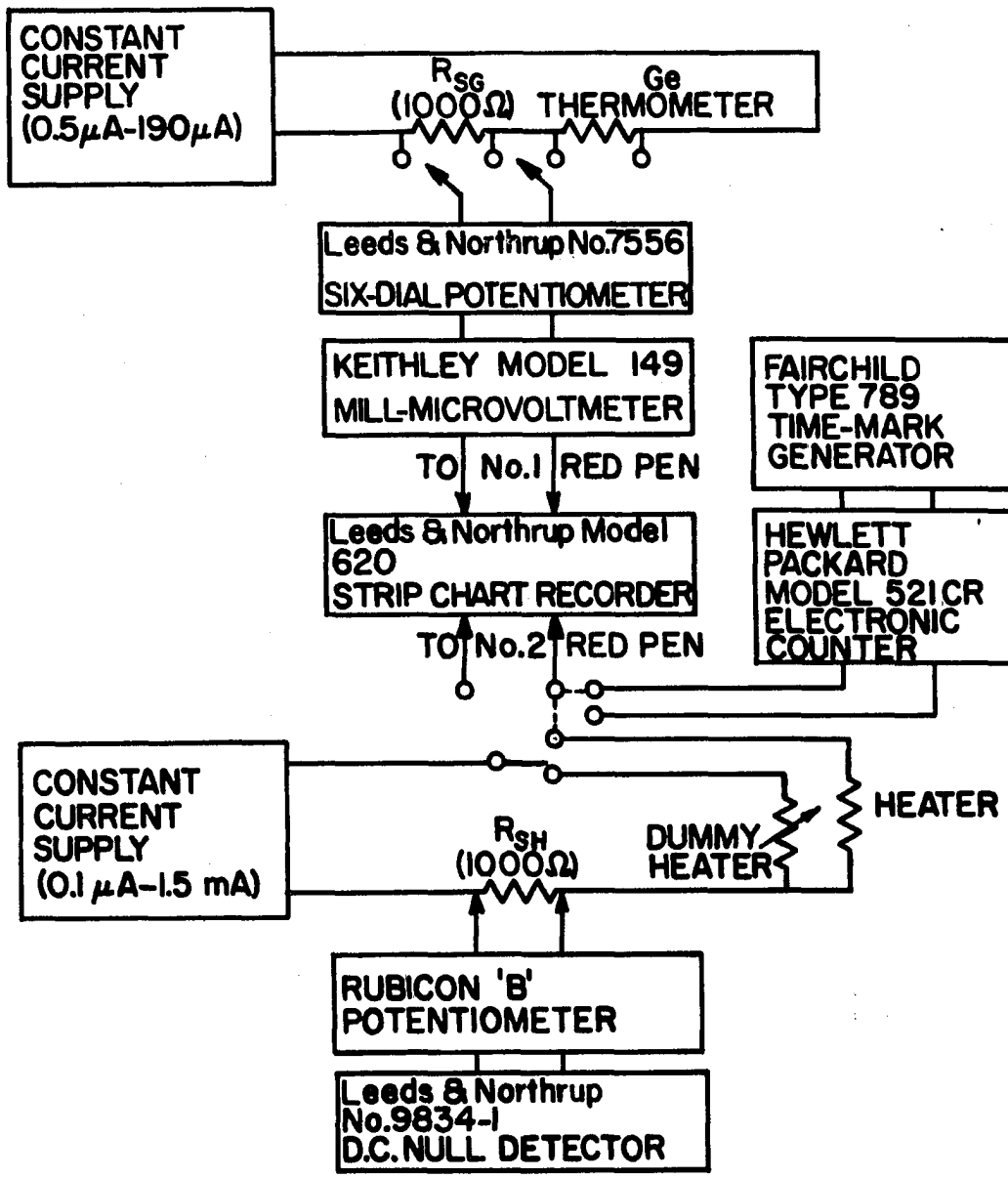

Figure 9. The block diagram of the electrical circuit for the heat capacity measurement

temperature $T_c(H)$ in various applied magnetic field H(H < 85 Oe). The R(H) values were obtained by dividing the voltage at the breaking point of the warming or cooling trace with the current passing through the Ge thermometer (I_G), and the $T_c(H)$ values were found from the pure thorium critical field $H_c(T)$ data reported by Dekker and Finnemore (33). The magnetic field produced magnetoresistance effect in the Ge thermometer. The correction to the temperature in the magnetic field was determined by noting the jump of the warming or cooling trace (ΔV) after applying a magnetic field. From the ΔV value, the change of temperature ΔT due to the magnetoresistance was obtained and the actual temperature T_0 was found to be $T_0 = T(H) + \Delta T$, where T(H) is the uncorrected temperature obtained in an applied field H. The correction was made for applied magnetic field up to 16 kOe.

The calibration data were divided into five overlapping temperature ranges. Using least square technique, data in each interval were fitted with a equation of the form

$$\ln T = A_0 + A_1(\ln R) + A_2(\ln R)^2 + \ldots \quad .$$

In order to ensure the continuity of two adjacent polynomials at the breaking point, the values of polynomial and their first derivatives were set equal at this point. The calibration of the Ge thermometer in detail has been reported by Bevolo et al. (34).

C. Measurements Procedure

Once the sample holder was clean, a sample was weighted and placed on the holder with 8 mg Apiezon N-grease to provide thermal contact.

The nylon threads and the copper wire were adjusted such that the sample holder was tightly stable in the center of the sample chamber and the copper wire was clamped tightly and completely free as the heat switch was closed and opened respectively. Then, the radiation shields were placed back and the inner cryostat was lowered carefully into the inner vacuum chamber. After the electrical leads and pumping lines were connected, the position of the inner cryostat was adjusted until the voltmeter, which was connected to a wire soldered on the 4 K shield and on the outer cryostat, indicated an open circuit. Once the 4 K shield did not touch the 77 K shield and the continuity of all electrical leads was tested, both the inner and outer vacuum chamber were evacuated.

When the pressure of both vacuum chambers reached approximately 10^{-4} Torr, the system was ready for cooldown. Once the nitrogen dewar and reservoir were full of liquid nitrogen, the inner vacuum chember was back filled with about 500 μm of nitrogen exchange gas. When the system was at about 77 K (normally in 8 hours), the nitrogen exchange gas was pumped out. As the pressure in the inner vacuum chamber was reduced to 10^{-6} Torr (in about 35 minutes), the system was ready for the transfer of liquid helium. Usually the first transfer of liquid helium lasted about 80 minutes and used about 22 liters of liquid helium.

A typical single data point was taken as follows. The heater current I_H and the thermometer current I_G were determined by measuring the voltage across the resistance R_{SH} and R_{SG} respectively. The total time of applying a heat pulse Δt was obtained by the reading of the counter (first digit and four numbers after the decimal point) and the

length of the trace of No.2 pen between the two jumps (second digit). A section of a strip chart recording form before and after applying the heat pulse is shown in Fig. 10. The voltage of the full chart was set to 100 μv, 30 μv or 10 μv for measurements of $T < 1.3$ K, $1.3 < 2.7$ K and $T > 2.7$ K respectively. After the slope of the initial drift trace of the No. 1 pen was straight for about 8 cm, the heater was turned on until the sample warmed up to the preset temperature which was usually less than 5% above the initial temperature. Then, the heater was turned off and the final drift trace was established. Voltage across the Ge thermometer before and after the applied heat pulse (V_i, V_f) were determined by extrapolating slopes of the initial and final traces to the vertical line passing through the midpoint of the heat pulse.

A computer program with inputs I_H, I_G, V_i, V_f, applied magnetic field H and the number of moles of the sample n was written to compute $\Delta Q = I_H^2 R_H \Delta t$, initial temperature T_i, final temperature T_f, average temperature $T = (T_i + T_f)/2$, T^2, temperature difference $\Delta T = T_f - T_i$, the total heat capacity $C = (\Delta Q/\Delta T)$, the molar sample heat capacity C and C/T. The molar sample heat capacity was obtained by dividing the difference between the total heat capacity and the addenda heat capacity by the number of moles of the sample. The addenda heat capacity was measured and fitted with least square technique. The best fit polynomials of the addenda heat capacity, the resistance of the heater, the resistance of the Ge thermometer and the correction of the resistance of the thermometer in a magnetic field were included as a subroutine.

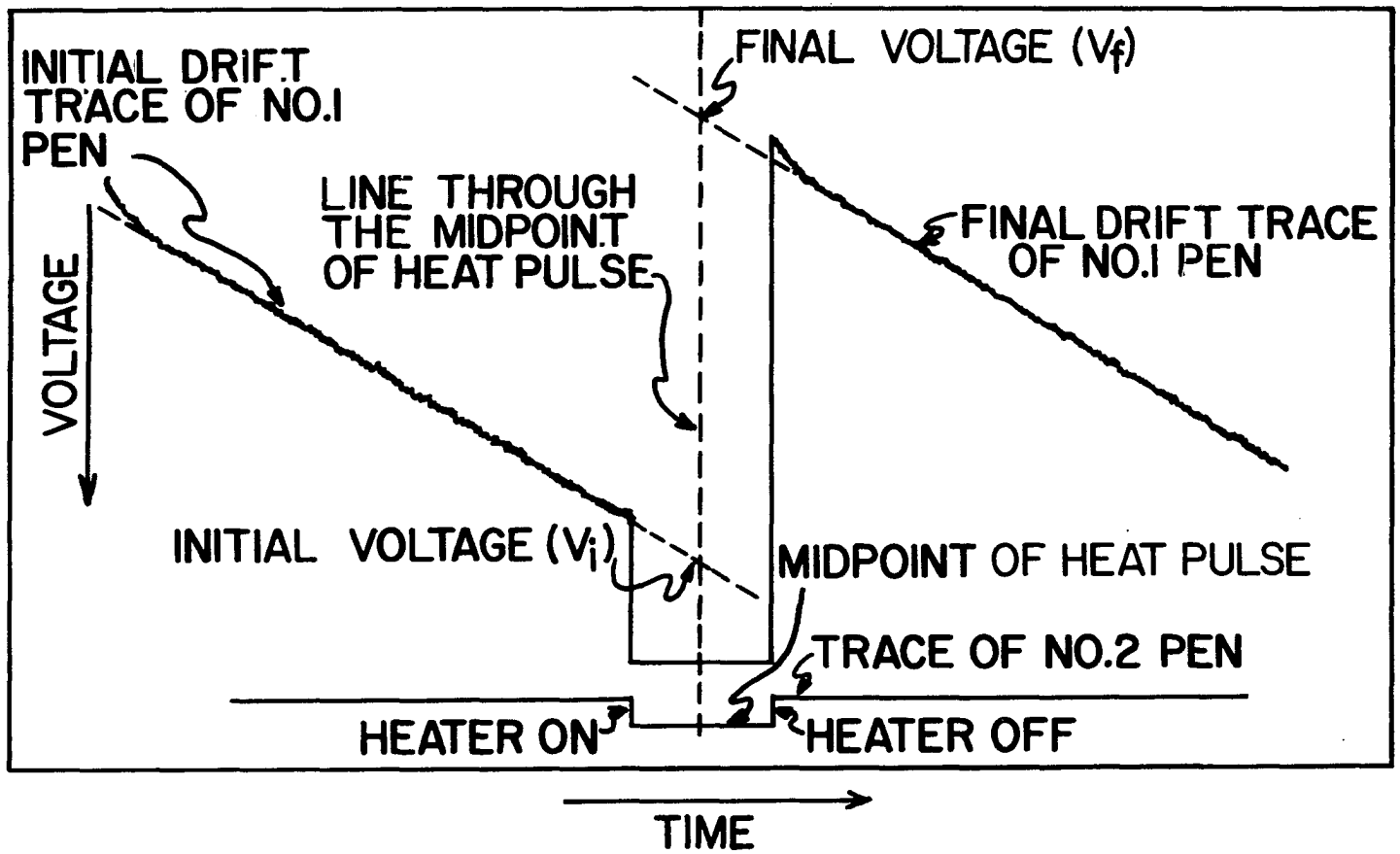

Figure 10. A section of strip chart recording form before and after an applied heat pulse

As suggested by Shanks (35), the thermal conductivity of the triclinic crystals along the a-c plane is at least ten times larger than that along the a-b or b-c plane. In order to obtain a faster thermal equilibrium after applying a heat pulse, several big regular triclinic crystals were picked out from the cluster of crystals. The flattest surface along the a-b or b-c plane was placed face down on the sample holder for thermal contact.

Since La is oxidized in air, the exposure time of La in air should be minimized. After 8 mg N-grease was placed on the sample holder directly instead of on the sample, the La sample surface was electropolished. It took about 10 minutes to complete the procedure from weighing the sample to evacuating the sample chamber.

In order to avoid trapping magnetic flux in the sample, all measurements from 1 K to 7 K with applied magnetic field were done as follows. The sample was cooled down from 7 K to 1 K in zero magnetic field, after which the desired magnetic field was applied slowly enough that the temperature did not rise above 1 K. Before the next set of data were taken, the field was reduced to zero and the sample was warmed up to 7 K. Then, the sample was cooled down to 1 K again in zero magnetic field and the desired magnetic field applied.

D. Preparation of Samples

Single crystal samples of sodium tungsten oxide ($Na_{0.33}WO_3$) and lithium tungsten oxide ($Li_{0.33}WO_3$) were prepared by H. R. Shanks by electrolysis of a fused salt (2). The Na_2WO_4-WO_3 and Li_2WO_4-WO_3 melts

containing about 65 mole % WO_3 were used for growth of $Na_{0.33}WO_3$ and $Li_{0.33}WO_3$ samples. For both samples, the growth temperature was kept within 5 C above the melting point of each melt. Single crystals were obtained from large clusters of intergrown crystals. The biggest single crystals were about 1 cm x 1 cm x 0.2 cm for $Na_{0.33}WO_3$ and 0.5 cm x 0.5 cm x 0.2 cm for $Li_{0.33}WO_3$.

The sodium-tungsten ratio from neutron activation analysis, and the parameters of the reduced unit cell of $Na_{0.33}WO_3$, as determined by x-ray diffraction, are given by B. H. W. S. de Jong (36) and are shown in Table 1. Since both $Na_{0.33}WO_3$ and $Li_{0.33}WO_3$ crystals were grown under nearly the same growth conditions and the phase diagram for the growth of $Li_{0.33}WO_3$ is very similar to that for the growth of $Na_{0.33}WO_3$, Shanks (35), based on the previous experience of growing these crystals, suggested that the reduced cell of $Li_{0.33}WO_3$ is only slightly different from that of $Na_{0.33}WO_3$ and the lithium concentration per formula weight of $Li_{0.33}WO_3$ is within 10% of 0.33.

Data from mass spectrographic analysis for both samples showed that the major impurities were alkali metals at a few thousand atomic ppm and Mo at several hundreds atomic ppm. The total other impurities are less than 100 atomic ppm.

Table 1. Analysis for the sodium tungsten oxide sample

Reduced cell						
a(Å)	b(Å)	c(Å)	W	Na	O	Formula
7.29	18.47	7.24	0.414	0.142	1.24	$Na_{0.34}WO_3$

The La sample was prepared in the Ames Laboratory by the Ca reduction of LaF_3 as described by Beaudry and Gschneidner, Jr. (37). The prepared La rod was purified by the solid state electrotransport (SSE) method by F. A. Schmidt. In this purifying process, a current density of about 380 A/cm^2 was used, and the pressure of the purifying system was kept about 10^{-10} Torr. It takes about 654 hours to complete this purifying process. After purification by SSE, the La rods were cooled down to room temperature very quickly, and then one of the rods was heat treated to obtain a single pure d-hcp phase. The samples for measurement were then cut from the center part of the electrotransported La rods.

Two samples, ET-1 and ET-2, which were prepared by B. J. Beaudry, were used in this study. The ET-1 sample which was cut from an La rod without heat treatment, consists of two half cylinder pieces. Each half cylinder is about 1 cm long and 0.14 cm^2 in cross section. The ET-2 sample obtained from a cold-worked La rod with a heat treatment as described by Legvold et al. (14), is a cylinder of about 1.5 cm long and 0.35 cm in radii. The ET-1 sample has about 1.95 grams, and the ET-2 sample has about 2.70 grams.

The analyses are shown in Table 2 for the batches of lanthanum before electrotransport. The only impurities analyzed for after SSE were O, N, and H by a vacuum fusion method. Sample ET-2 was analyzed for O, N, and H after the heat treatment to produce the pure d-hcp phase.

Table 2. Analyses[a] of the La samples in atomic ppm (Weight ppm in parentheses)

Impurity	ET-1	ET-2	JF[b]
H	138 (1)	276 (2)	(12)
O	87 (10)	78 (9)	(118)
N	10 (1)	10 (1)	____[c]
C	139 (12)	92 (8)	(170)
F	88 (12)	180 (25)	____
Fe	7 (2.9)	4 (1.7)	____
Ni	4	< 0.6	____
Cu	0.67	1.8	(40)
Ta	3.7	2	(<500)
Ce	4	1	____
Gd	< 5	< 0.6	____
Y	4	< 0.6	____
Si	< 0.83	2	____
Cl	2	10	____

[a]All metallic impurities were determined by mass spectrometry (those not listed were present in less than 1 ppm); H, O, and N by vacuum fusion; C by a combustion-chromatography method; and F by the formation, distilled, and determination of fluosilicic acid method.

[b]Normal d-hcp La reported by Johnson and Finnemore (19).

[c]____: not determined.

IV. RESULTS

A. Copper

Before measuring any samples, the heat capacity of a sample of 99.999% American Smelting and Refining Company copper was measured for a test of the overall accuracy. These copper data, compared to the NBS copper compilation (38) for $30 < T < 60$ K, agreed within 0.3% at 30 K and 0.65% at 60 K. From 1 K to 30 K, the copper data were compared to the copper equation from Hoiste, Cetas, and Swenson (HCS) (39). The deviation of the copper results from the HCS values were found to lie within 0.35% of HCS for $20 < T < 30$ K, 0.2% of HCS for $3 \text{ K} < T < 20$ K and 1% of HCS from 1 K to 3 K. These results are in good agreement with the measurements reported by Bevolo et al. (34).

B. Triclinic Sodium and Lithium Tungsten Oxide Crystals

At sufficiently low temperature the heat capacity in the normal state usually has

$$C_p = \gamma T + \beta T^3 \ . \tag{4.1}$$

Where γT is the electronic heat capacity and βT^3 is the Debye lattice heat capacity. When the data are plotted as C/T vs. T^2 Equation (4.1) predicts a straight line with slope β and intercept γ. The Debye temperature θ_D can be obtained by the relation

$$\theta_D = \left[\frac{r \times 1.944}{\beta}\right]^{1/3} \times 100 \tag{4.2}$$

here β is units of mJ/mole-K^4 and r is the total number of atoms per formula weight. In order to compare results with the hexagonal bronzes, the same value of $r = 4 + x = 4.33$ was used for both triclinic samples.

The heat capacity data for $Na_{0.33}WO_3$ and $Li_{0.33}WO_3$ are plotted as C_p/T vs. T^2 in Fig. 11 and Fig. 12, and as C_p vs. T in Fig. 13. For all measurements of both samples, the applied magnetic field was less than 1 Oe and no superconducting behavior was found down to 1 K for either sample.

Data for $Na_{0.33}WO_3$ and $Li_{0.33}WO_3$ for $1 < T < 6.3$ K are illustrated in Fig. 11. Both sodium and lithium tungsten oxide show a linear behavior on a C/T vs. T^2 plot until the temperature reached about 3.5 K and 4.0 K respectively. Using least square techniques, the best fit equation to the data from 1 K to 3 K is $C/T = 0.011 + 0.388\ T^2$ for $Na_{0.33}WO_3$ and $C/T = 0.408 + 0.213\ T^2$ for $Li_{0.33}WO_3$ where the units for the constant term are in mJ/mole-K and the units for the coefficient of T^2 term is in mJ/mole-K^3. Since both triclinic samples are semiconductors (3, 35), it is expected that the γ value of $Na_{0.33}WO_3$ is nearly zero, but the origin of $\gamma = 0.408$ mJ/mole-K for $Li_{0.33}WO_3$ is unknown. From β values, the Debye temperature was found to be $\theta_D = 279 \pm 2$ K for $Na_{0.33}WO_3$ and $\theta_D = 341 \pm 3$ K for $Li_{0.33}WO_3$.

Fig. 12 shows the results for $Na_{0.33}WO_3$, $Li_{0.33}WO_3$ and published data (8) of WO_3 and cubic Na_xWO_3 for $1 < T < 20$ K. The data of both triclinic samples are drastically different from that of WO_3 and cubic Na_xWO_3. It is clear that the heat capacity of $Na_{0.33}WO_3$ and $Li_{0.33}WO_3$

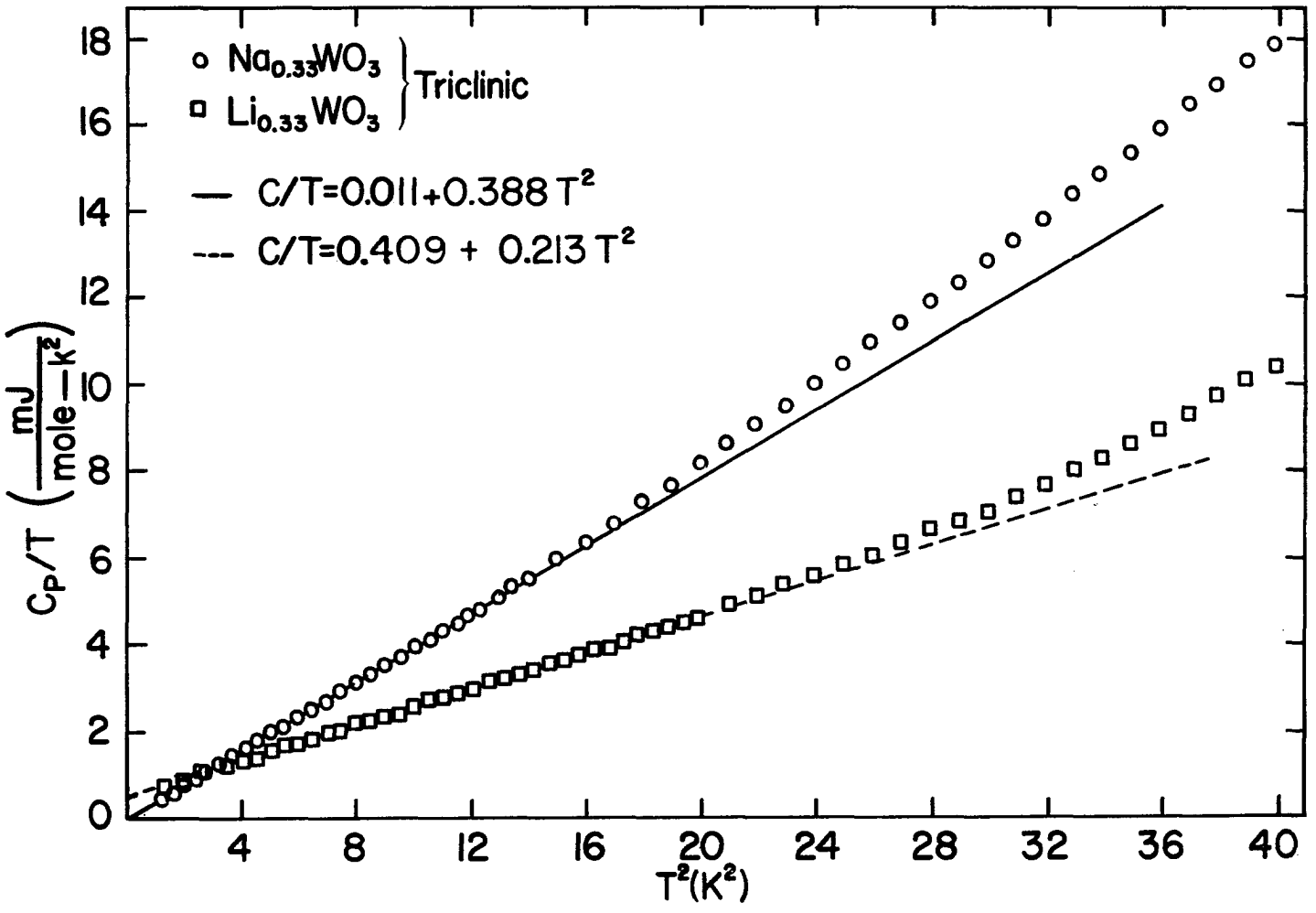

Figure 11. Heat capacity of the triclinic $Na_{0.33}WO_3$ and $Li_{0.33}WO_3$ crystals for $1 < T < 6.3$ K

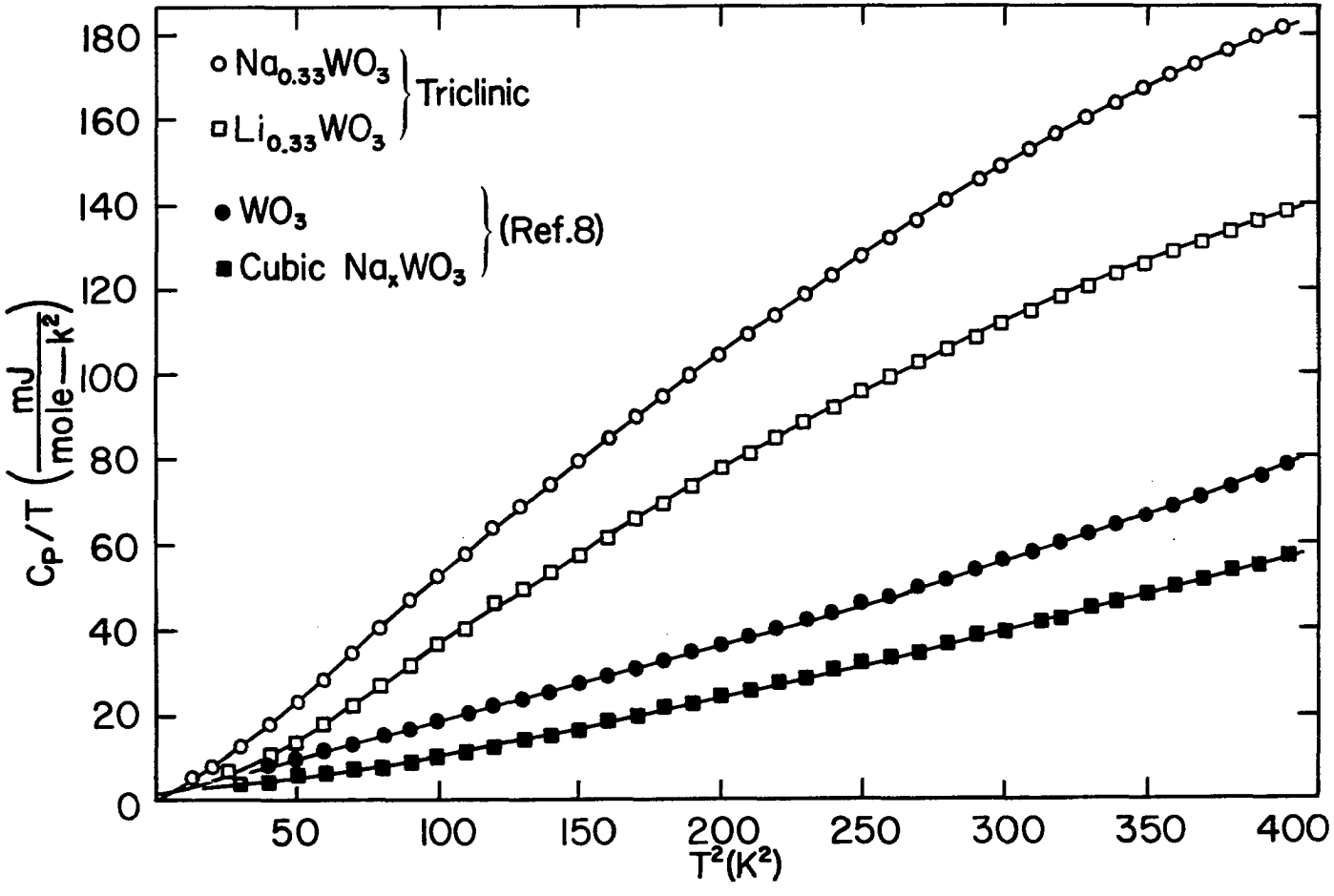

Figure 12. Heat capacity of the triclinic $Na_{0.33}WO_3$ and $Li_{0.33}WO_3$ crystals, WO_3 and cubic Na_xWO_3 for 3 K < T < 20 K

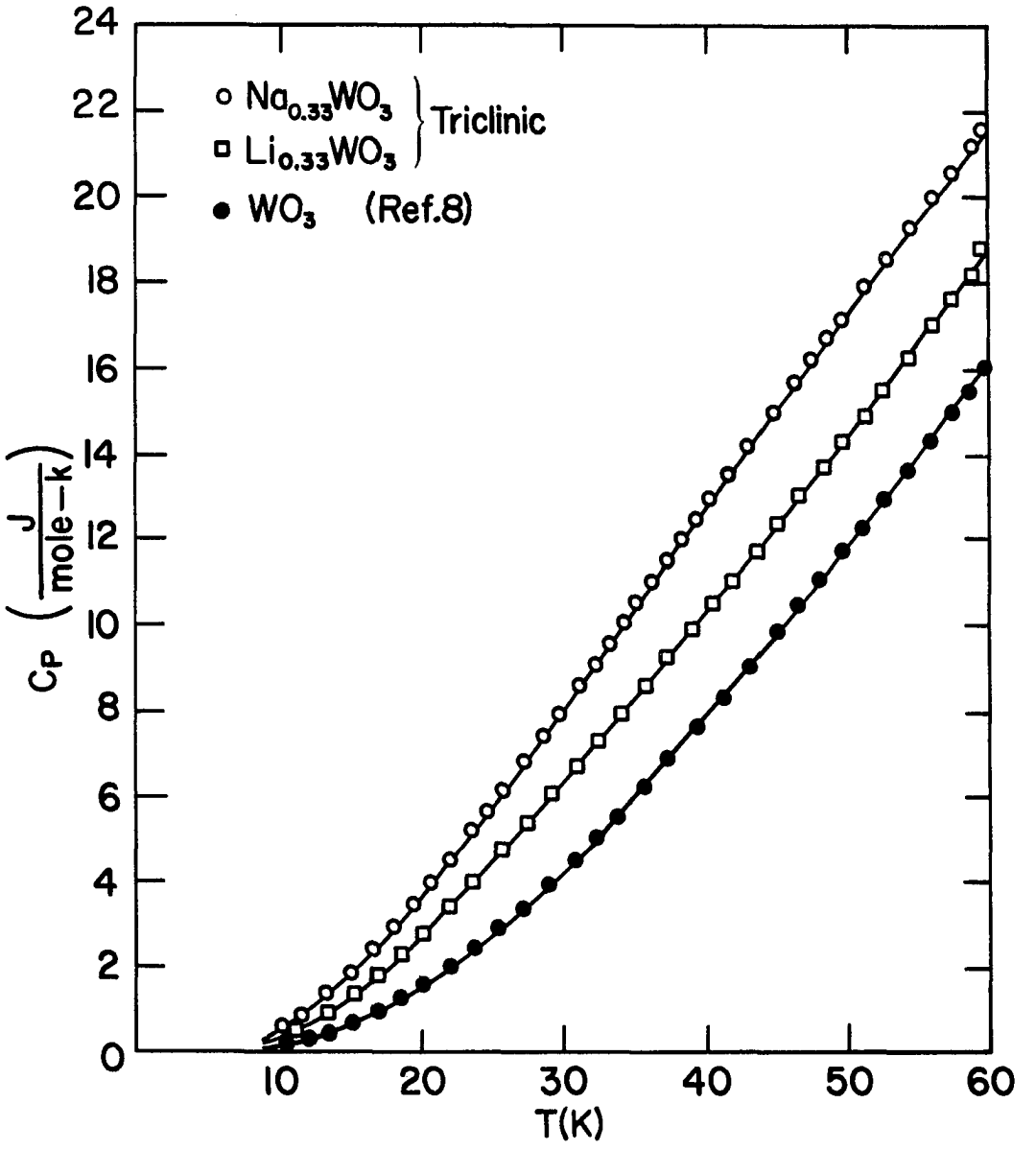

Figure 13. Heat capacity of the triclinic $Na_{0.33}WO_3$ and $Li_{0.33}WO_3$ crystals and WO_3 for $1 < T < 60$ K

show a conspicuous excess heat capacity with respect to the heat capacity of WO_3.

The data of triclinic samples and WO_3 are shown in Fig. 13 for temperatures up to 60 K. As shown in Fig. 14, above 55 K and 50 K respectively, the difference between the heat capacity of $Na_{0.33}WO_3$ and the heat capacity WO_3, and the difference between the heat capacity of $Li_{0.33}WO_3$ and the heat capacity WO_3, is nearly independent of temperature. This result would be expected, if the difference is due to an Einstein mode.

C. Lanthanum

The heat capacity of La from 1 K to 7 K is shown in Fig. 15 for the ET-1 sample, and in Fig. 16 for the ET-2 sample. For both samples, there is a sharp rise in the zero-field heat capacity at about 5 K indicating a superconducting transition of the La metal with majority of the d-hcp phase. A small shoulder at about 6 K was also found for the zero-field data of the ET-1 sample, with indicates the presence of a few percent of the fcc phase in this sample. When the jump of heat capacity ΔC, the transition temperature T_c, and the width of the transition ΔT_c are determined by the conventional method shown in Fig. 17, the values shown in Table 3 are found. At lower temperatures (1 K to 2.9 K), the data with an applied field (10 kOe) for both samples showed a linear behavior on the C/T vs. T^2 plot. Using the least square technique, the best fit of the data of each sample to the equation $C/T = \gamma + \beta T^2$ provided $\gamma = 9.58$ and $\beta = 0.58$ for the ET-1 sample, and

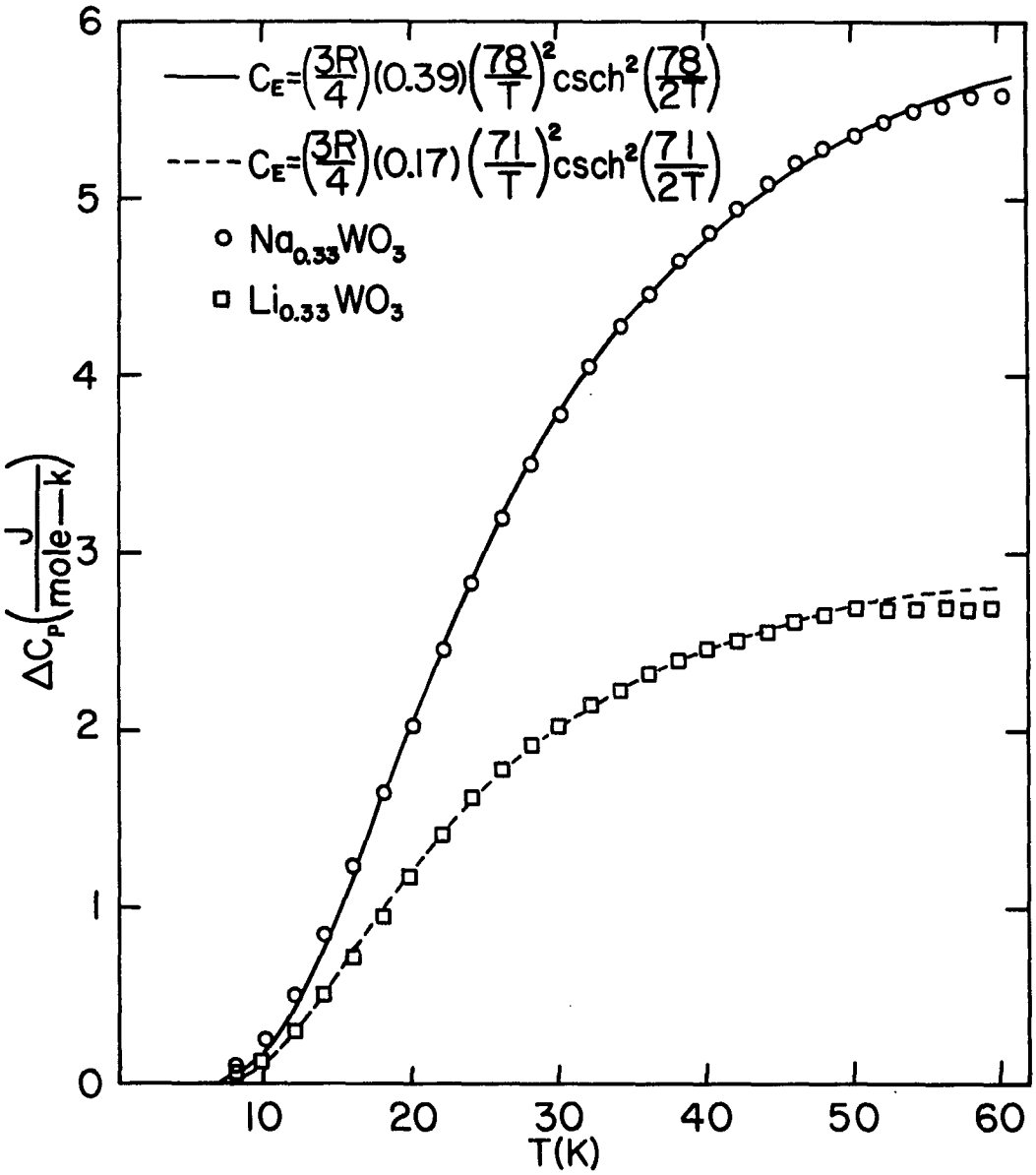

Figure 14. The excess heat capacity of the triclinic $Na_{0.33}WO_3$ and $Li_{0.33}WO_3$ samples vs. temperature. The excess heat capacity ΔC is defined as C_g(sample) - $C_g(WO_3)$, where C_g is the lattice heat capacity

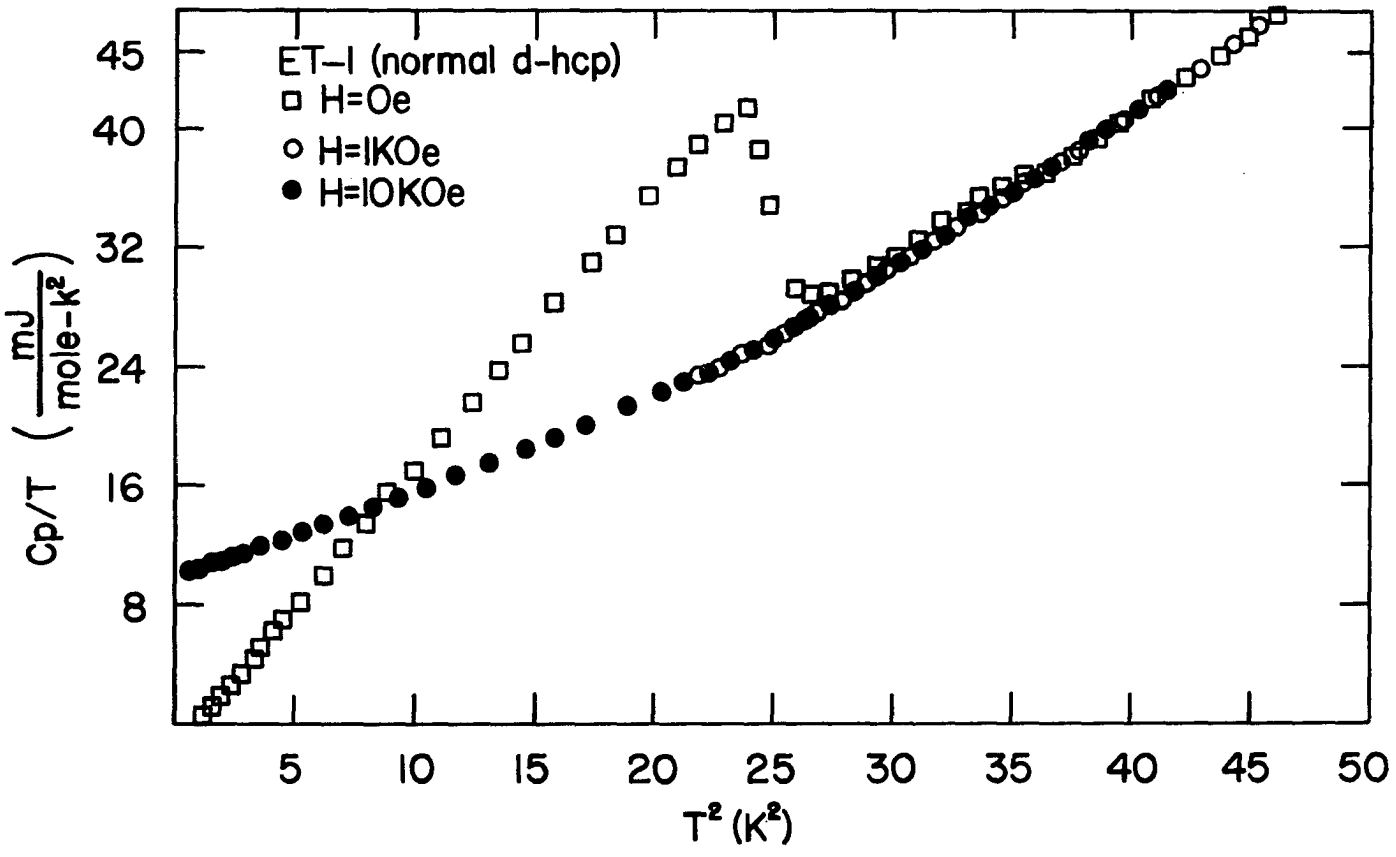

Figure 15. Heat capacity for the ET-1 sample (normal d-hcp phase) from 1 K to 7 K (C_p/T vs. T^2)

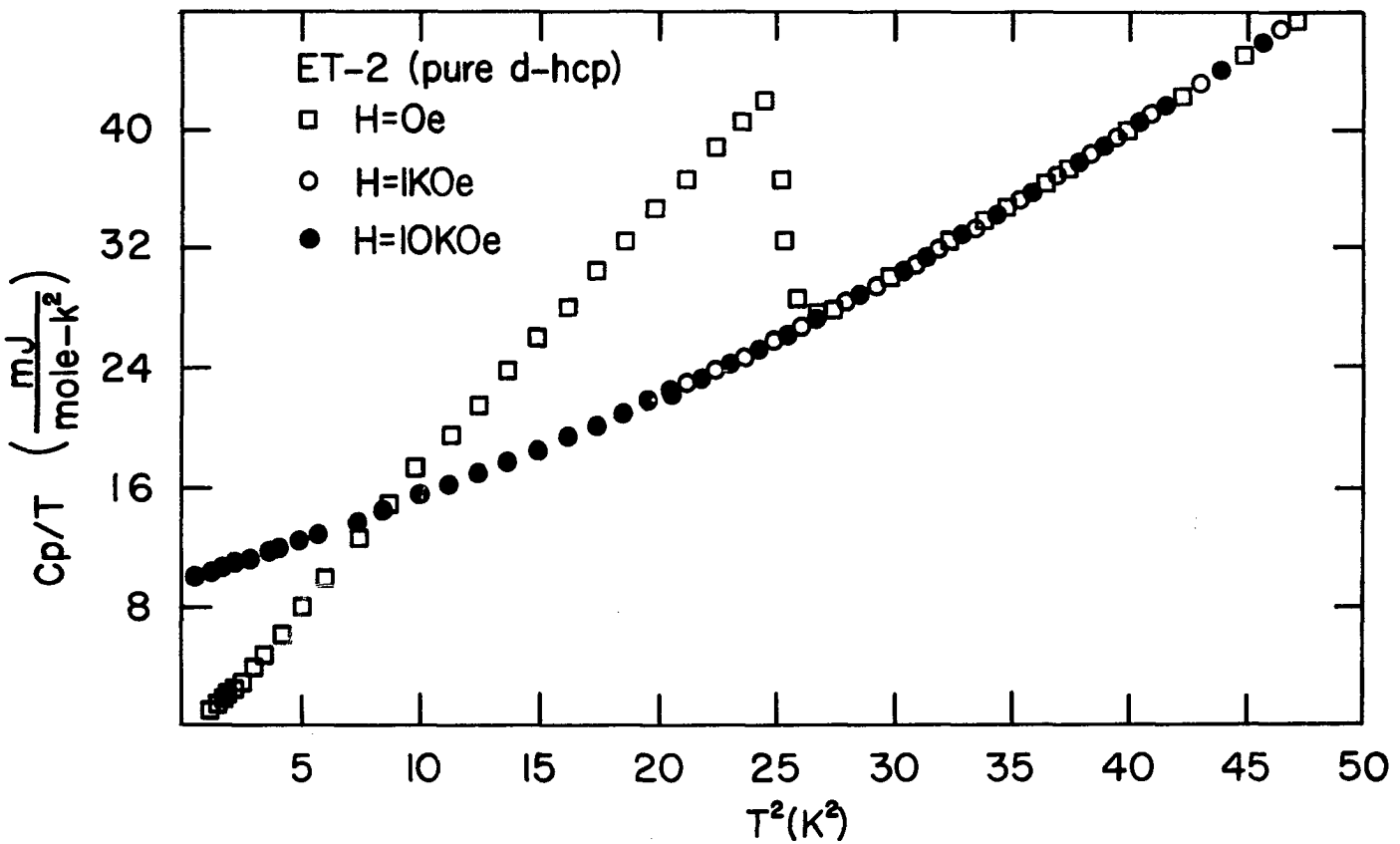

Figure 16. Heat capacity for the ET-2 sample (pure d-hcp phase) from 1 K to 7 K (C_p/T vs. T^2)

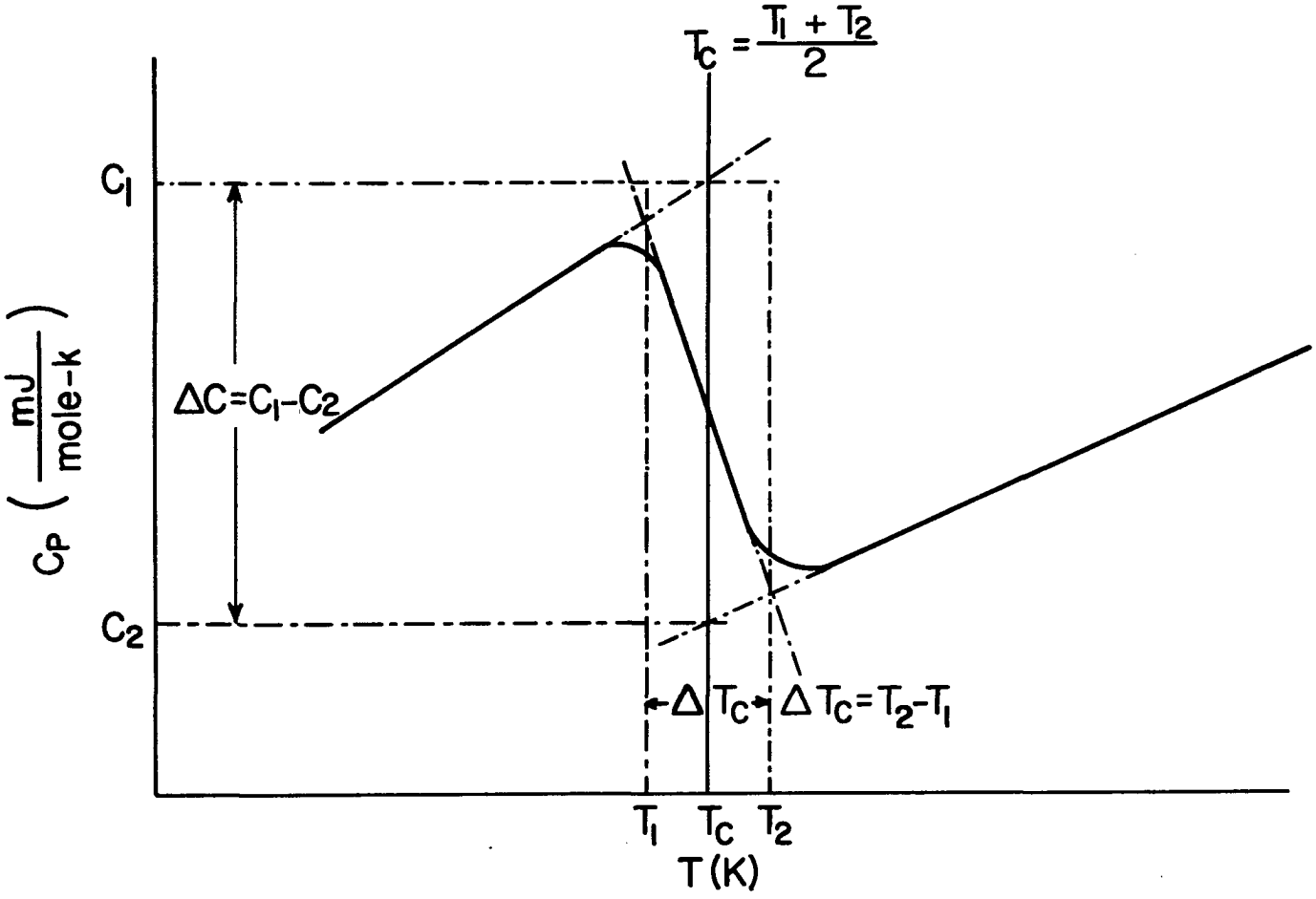

Figure 17. Method of determining the jump of heat capacity ΔC, the transition temperature T_c, and the width of superconducting transition ΔT_c

Table 3. The percent of d-hcp phase f, the transition temperature T_c, the width of the transition ΔT_c, and the jump in the heat capacity ΔC for the ET-1 and ET-2 samples

		ET-1	ET-2
f	(%)	92.7 ± 1	> 99
$T_{c\alpha}$[a]	(k)	4.98 ± 0.03	5.04 ± 0.02
$T_{c\beta}$[a]	(k)	6.02 ± 0.07	
$\Delta T_{c\alpha}$[a]	(k)	0.15 ± 0.02	0.1 ± 0.01
$\Delta T_{c\beta}$[a]	(k)	0.25 ± 0.04	
ΔC_{α}[a]	(mJ/mole-K)	78.85 ± 4	85 ± 2
ΔC_{β}[a]	(mJ/mole-K)	9.1 ± 5	

[a]The subscripts α and β indicate the α and the β phase respectively.

γ = 9.45 and β = 0.57 for the ET-2 sample, where γ is in units of mJ/mole-K^2, and β is in units of mJ/mole-K^4. From the β value, one finds that θ_D = 151 K for the ET-1 sample, and θ_D = 150 K for the ET-2 sample.

The absence of a small shoulder at about 6 K for the ET-2 sample suggested that this sample is almost entirely the d-hcp phase. In order to determine the percent quantitatively, four sets of data from 5.2 K to 6.6 K were tested. Two of these four sets were measured in zero field, the rest were obtained in an applied field, one in 1 kOe and another in 10 kOe. The maximum deviation of the zero-field data from the data taken in a magnetic field was found to be 0.55%. The average heat capacity at 6 K for these four sets is 214.5 mJ/mole-K, so the value of the maximum deviation at 6 K is 1.18 mJ/mole-K, which is less than 1% of the jump of heat capacity for the pure fcc La (ΔC_β = 120 mJ/mole-K) reported by Johnson and Finnemore (JF) (19). This result suggested that the ET-2 sample has at least 99% of the d-hcp phase. Because the deviation of the zero-field data from the data in an applied field is not systematically high for temperatures from 5.2 K to 6.6 K, but is random in the whole tested temperatures range from 5.2 K to 6.6 K, it is reasonable to assume that the ET-2 sample has a pure d-hcp structure. Based on this assumption, the heat capacity of the pure d-hcp La can be obtained directly from the data of the ET-2 sample.

When one further assumes that the jump in the heat capacity ΔC at the transition temperature T_c is proportional to the relative amount of

each phase present in the sample, the percent of the d-hcp phase f in the ET-1 sample was found to be f = 78.9/85 = 92.4%. Because the fraction of fcc metal is very small in the ET-1 sample, the determination of the properties of the fcc phase is much less accurate than for the d-hcp phase. The data for the pure fcc La were not estimated here.

The zero-field heat capacity for both samples from 7 K to 60 K are shown in Fig. 18. From this rather coarse C vs. T plot, both sets of data fall approximately on the same curve. A closer check of these data reveals that the difference between the ET-1 data and ET-2 data is nearly a constant over the whole temperature range. Comparing the JF data from 7 K to 10 K with the ET-1 data and the ET-2 data, one finds that the JF sample lies between the ET-1 data and the ET-2 data. Because the ET-1 sample, the JF sample and the ET-2 sample has 93%, 96% and > 99% of the pure d-hcp phase respectively, this result is expected and shows an agreement between the measurement reported here and that reported by JF.

From the ET-2 data in the normal state, the temperature dependent Debye temperature θ_D (T) for the pure d-hcp La from 1 K to 30 K were obtained and shown in Fig. 19. A closer look at this figure reveals that θ_D (T) is nearly temperature independent up to about 2.9 K. This result agrees with the prediction of Blackman (40) that θ_D will remain constant for temperatures below $\theta_D/50$. A minimum in θ_D (T), which occurred at about 11.1 K, was also found here.

As shown in Fig. 20, the jump in the heat capacity, ΔC, at T_c for the pure d-hcp La is ΔC_α = 85 ± 2 mJ/mole-K, or 1.78 ± 0.04 $\gamma_\alpha T_{c\alpha}$.

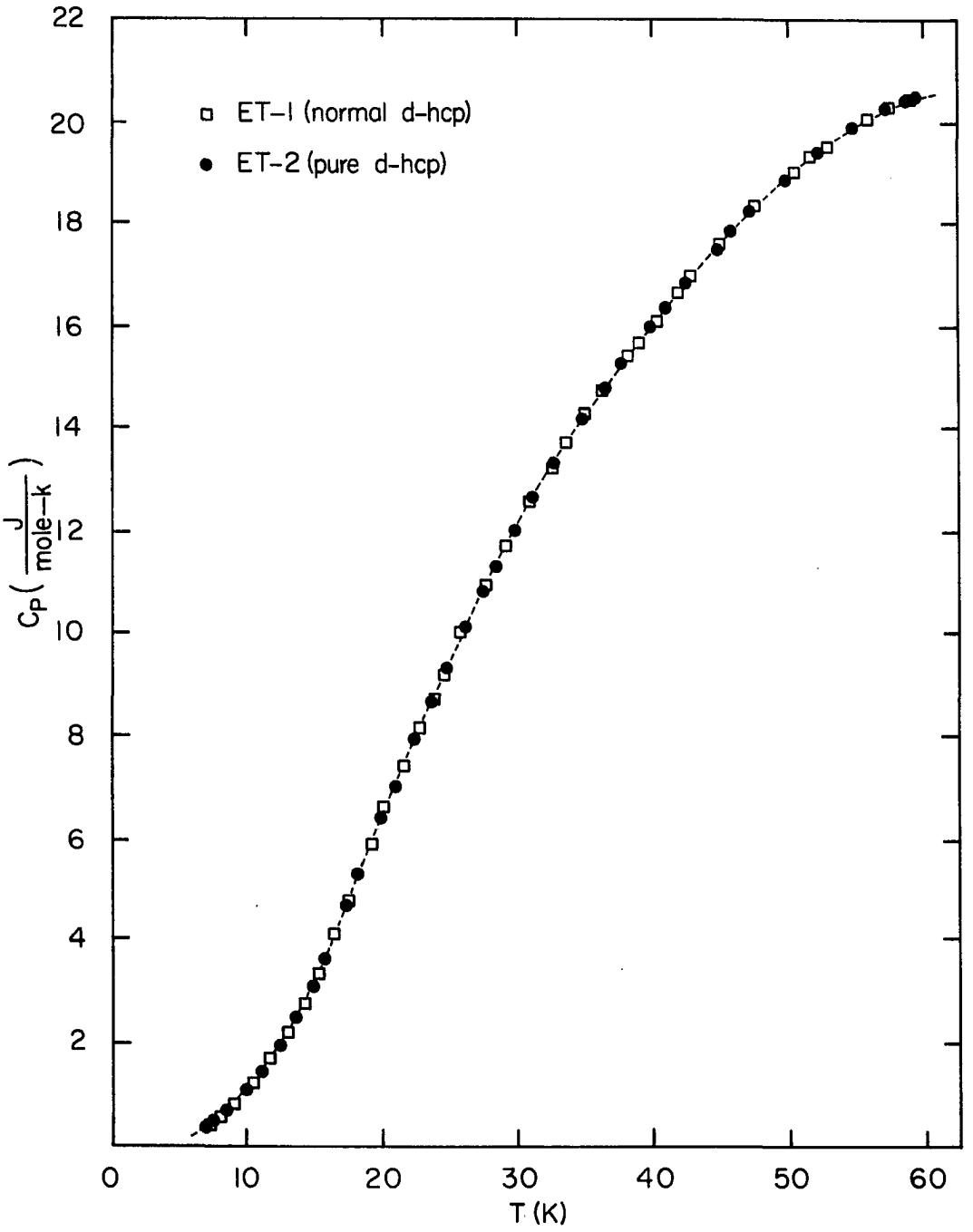

Figure 18. Heat capacity for the ET-1 and ET-2 samples from T = 7 K to 60 K (C_p vs. T)

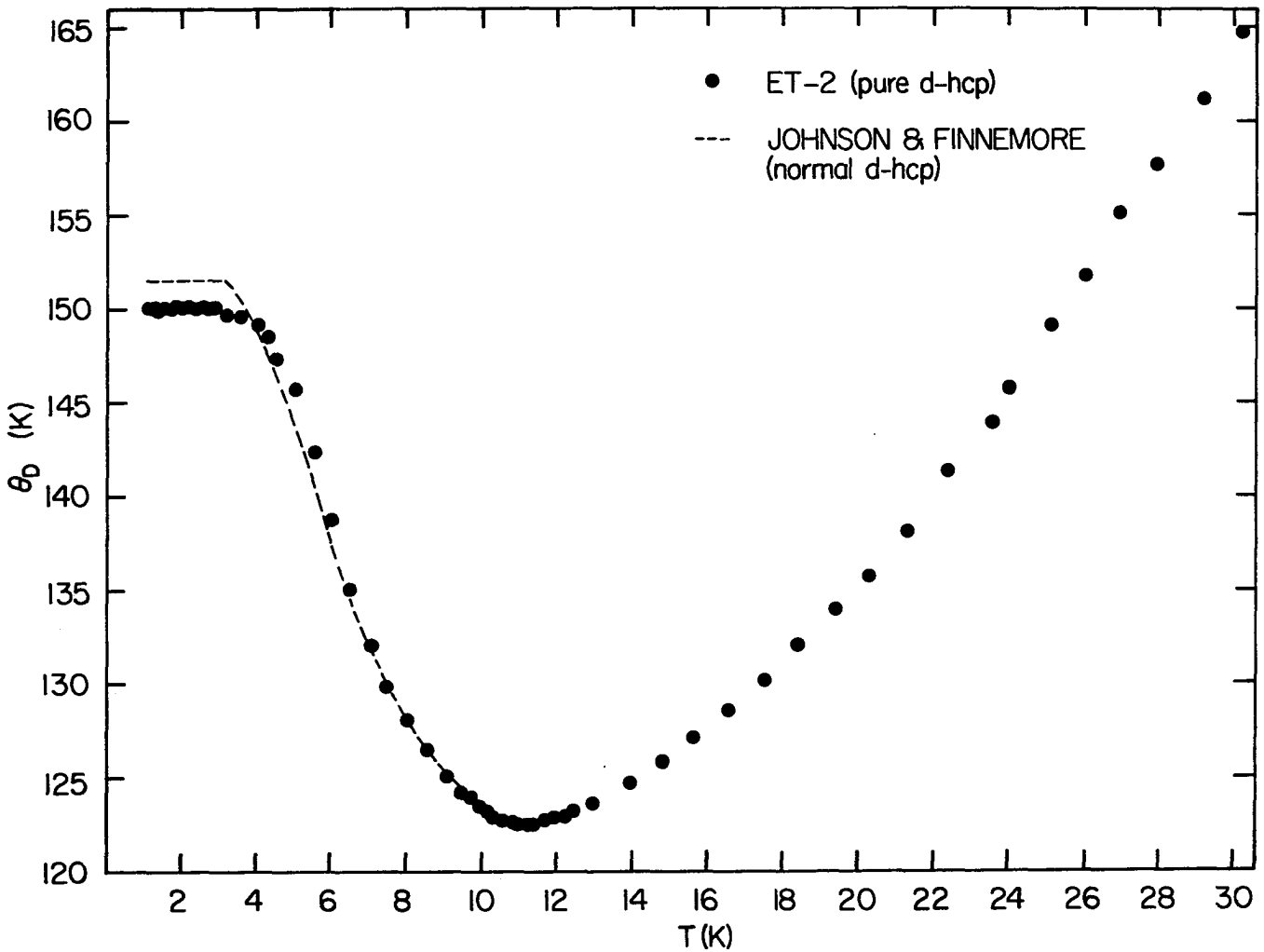

Figure 19. Debye temperature θ_D as a function of temperature for the pure d-hcp La (θ_D vs. T)

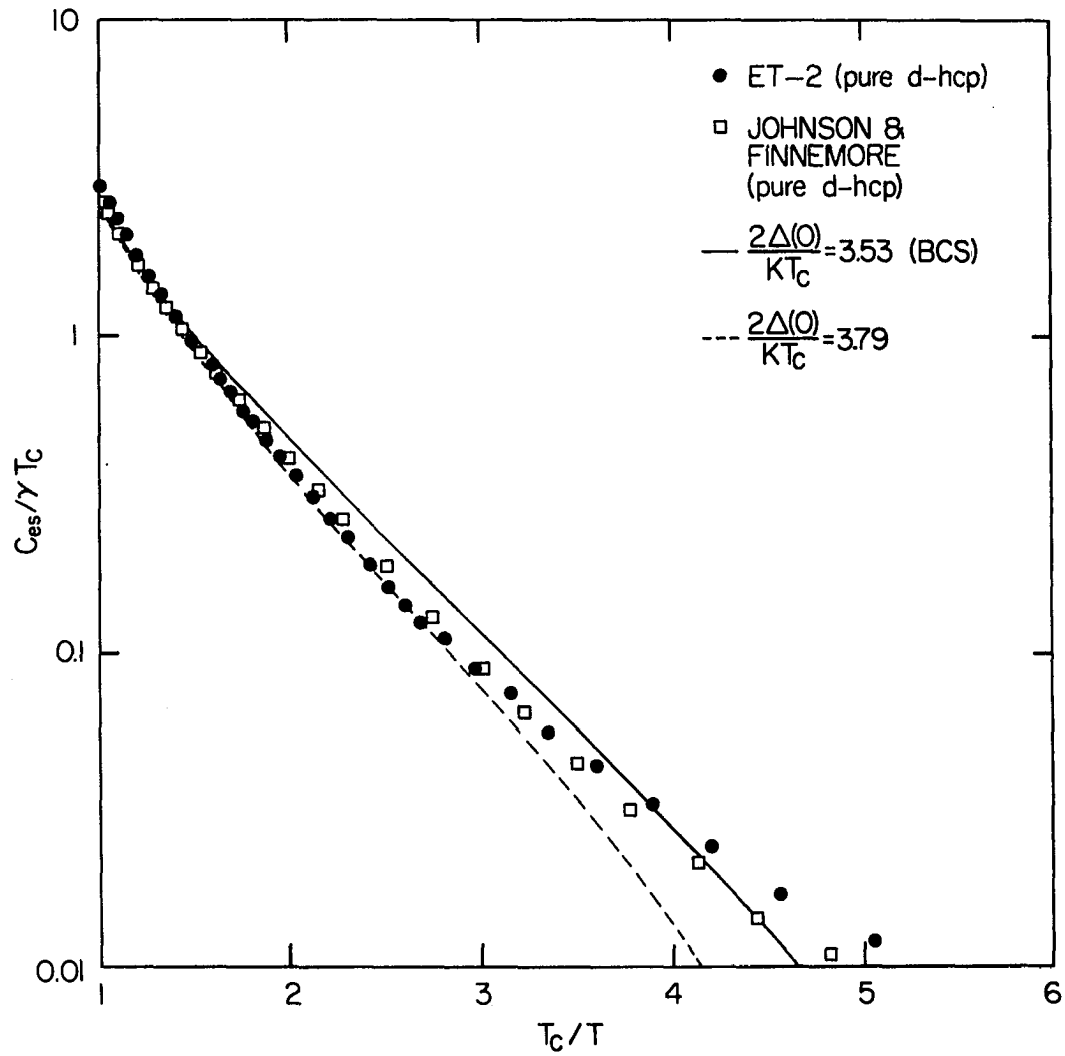

Figure 20. Reduced superconducting electronic heat capacity of the pure d-hcp La ($\ln(C_{es}/\gamma T_c)$ vs. T_c/T)

This value is higher than the BCS value of $\Delta C = 1.43\ \gamma T_c$. The jump in the heat capacity for the pure fcc La can be obtained by dividing the ΔC value of the ET-1 data at $T = T_{c\beta} = 6.02$ K by the percent of the pure fcc phase in this sample. The value of ΔC_β is found to be 125 ± 12 mJ/mole-K, or $1.83 \pm 0.18\ \gamma_\beta T_{c\beta}$. Because the zero-field ET-1 data have larger scattering near T = 6 K, the uncertainty in determining ΔC_β increases to 10%.

From the discussion in Chapter II, the electronic specific heat in the superconducting state C_{es} can be determined from the relation $C_{es} = C_s - C_N + \gamma T$. The calculated C_{es} data from this relation for the ET-2 samples and for the pure d-hcp La reported by JF are shown on a $\ell n(C_{es}/\gamma T_c)$ vs. T_c/T plot in Fig. 20. The curve predicted by BCS theory and the best fit curve to the ET-2 data, which were obtained by scaling the temperature-dependent BCS energy gap by a constant factor as suggested by Finnemore and Mapother (41) are also shown in Fig. 20. For the pure d-hcp La, the value $2\Delta(0)/k_B T_c = 3.79$ gives the best fit to the data between 1.4 K and 3.6 K. The obtained energy gap is larger than the BCS prediction of 3.53.

The thermodynamic critical field $H_c(T)$ can be determined by the relationship

$$G_N(T) - G_S(T) = \int_T^{T_c} [S_N(T) - S_S(T)]dT = -(\frac{V}{8\pi})(H_c(T))^2 \qquad (4.3)$$

The entropy $S_i(T) = \int_0^T (C_i(T)/T)dT$ was obtained by using planimeter to measure the area under the curve on a large scale graph of $C_i(T)/T$ vs. T,

where i denotes the normal (N) or the superconducting (S) state. As the temperature ranged from T = 0 K to T = T_c, the total entropy in the normal state was found to be equal to the total entropy in the superconducting state within 0.5%. This result agrees with the prediction of the third law of thermodynamic within experimental error. Using the values of the entropy difference, Equation (4.3) was integrated graphically and the $H_c(T)$ value was obtained by using the value V = 22.54 cm^3/mole (42). The critical field at T = 0 was found to be $H_c(0)$ = 840.4 Oe for the pure d-hcp La, which is about 5% higher than the value reported by JF. From Fig. 21, one finds that the $H_c(T)$ values for the ET-2 sample fit the relation, $H_c(T) = H_c(0)[1 - T^2/T_c^2]$ within 0.2%. One also finds that the value of $(dH_c(T)/dT)$ at T = T_c is 333 Oe/K which is about 8% higher than the value obtained by the Rutger relation (27):

$$\left(\frac{dH_c(T)}{dT}\right)_{T=T_c} = \left(\frac{4\pi\Delta C}{VT_c}\right)^{1/2} = 306\ \frac{Oe}{K}\ .$$

For a comparison with theory, it is convenient to plot the deviation function of the critical field $D(t) = H_c(T)/H_c(0) - (1 - t^2)$ of the data and the theory on D(t) vs. t^2 graph. Fig. 22 shows that the ET-1 data and the ET-2 data lie between the deviation curves for mercury and tin reported by Finnemore and Mapother (41), with D(t) being less than 0.0003. Curves obtained by scaling the temperature-dependent BCS energy gap by factors of 3.90/3.53 and 3.84/3.53 give a best fit to the ET-1 and the ET-2 data respectively. These best fit curves suggested

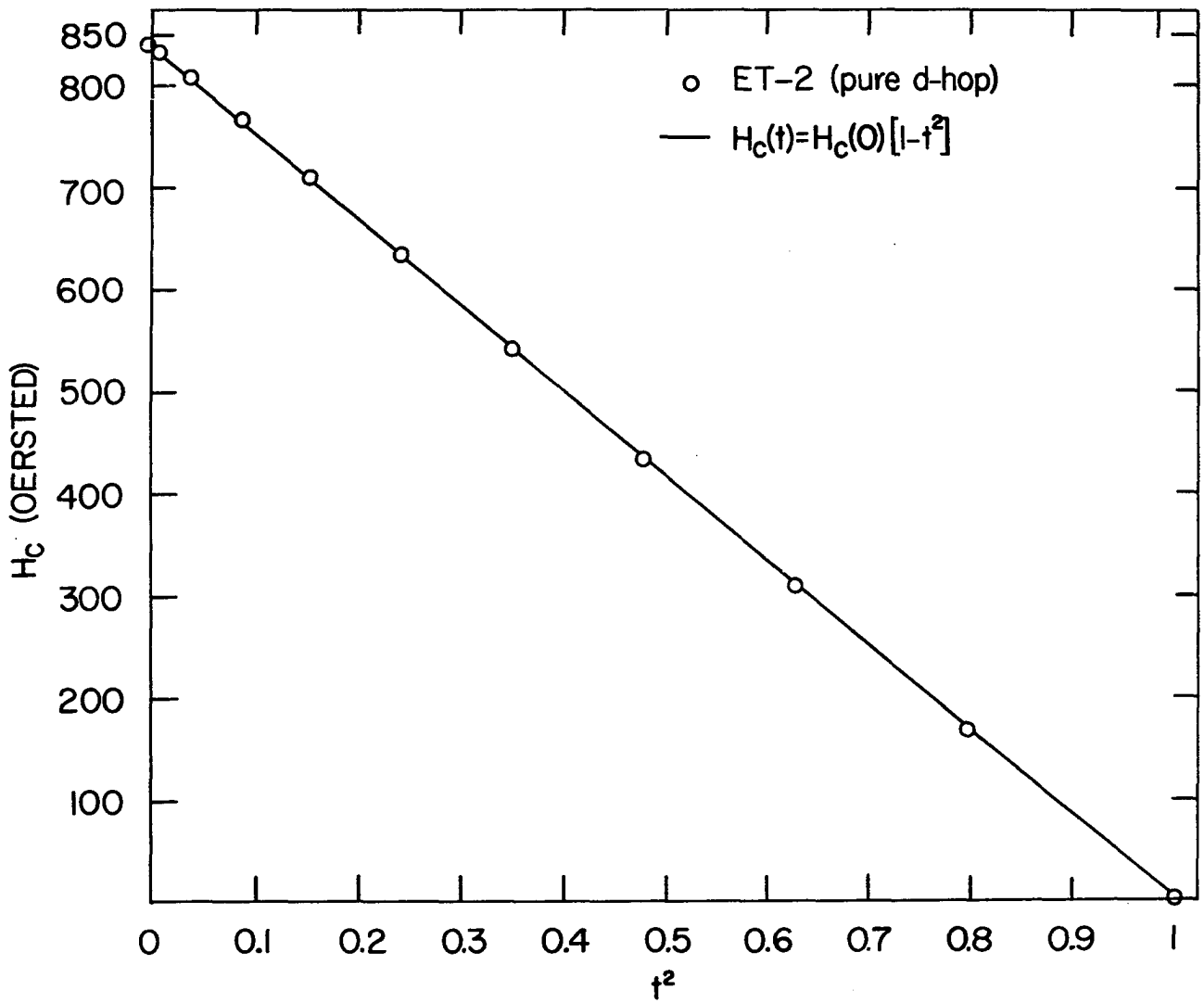

Figure 21. Thermodynamic critical field $H_c(T)$ of the pure d-hcp La vs. t^2, where $t = T/T_c$

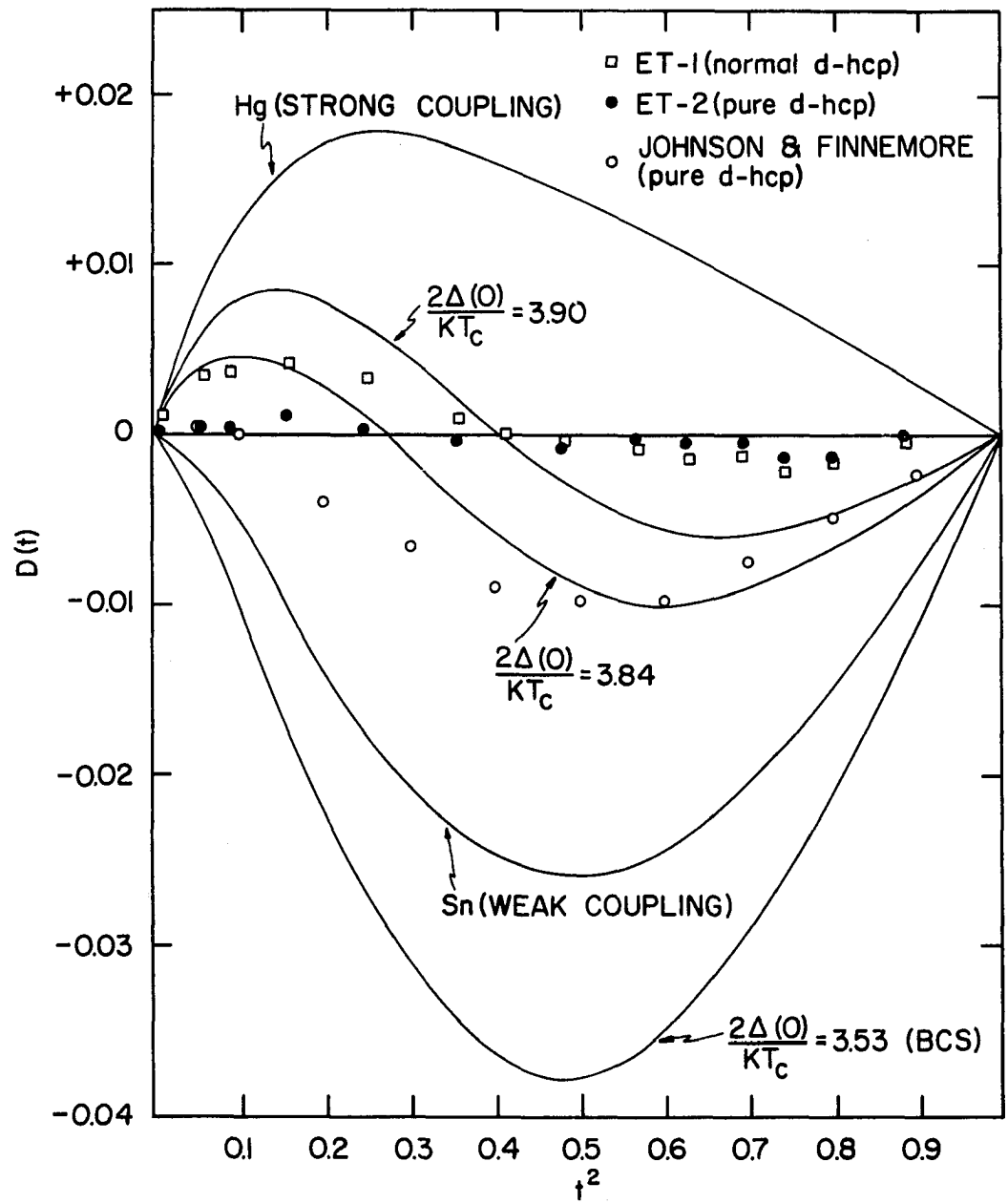

Figure 22. Deviation of the critical field of the ET-1 and ET-2 samples vs. t^2, where $t = T/T_c$

an energy gap of 3.84 $K_B T_c$ for the pure d-hcp La, and an energy gap of 3.90 $K_B T_c$ for the normal d-hcp La with 9% d-hcp phase.

According the Goodman (43), the value of the energy gap at T = 0 K can be obtained from the relation $2\Delta(0)/K_B T_c = [2\pi V H_c(0)^2/3\gamma T_c^2]$. Using the values of $H_c(0)$, γ, T_c, and V shown in Table 6, the energy gap for the pure d-hcp La was found to be $2\Delta(0)/K_B T_c = 3.73$. This value is in good agreement with the best fit value of the $C_{es}/\gamma T_c$ data in Fig. 21. As discussed in Chapter II, the value of the attractive interaction between the electron pair in the superconductor, V_p, can be determined from the relations $\gamma = 2/3\pi^2 K_B N(0)$ and $T_c = 1.14\ \theta_D \exp [1/N(0)V_p]$. Using the obtained values of γ, T_c, θ_D, the magnitude of V_p was found to be 0.143 eV. This value is about 2% higher than the value reported by JF.

For the temperature near 5 K, the heat capacities of the ET-2 sample in the 5 Oe and 10 Oe applied magnetic fields are shown in Fig. 23. From this C/T vs. T^2 plot, it is clear that there isn't any sharp peak present in the heat capacity with a small applied field. A closer look at this figure reveals that the transition width increases slightly when increasing the small applied field. The results indicate the absence of a latent heat associated with the superconducting transition in a small field.

The behavior of the specific heat in a magnetic field are complicated somewhat by the demagnetization effect. For a cylinder with the axis perpendicular to the field and with the ratio of the axis to the radii being 0.23, the demagnetization factor is about 0.7 and the

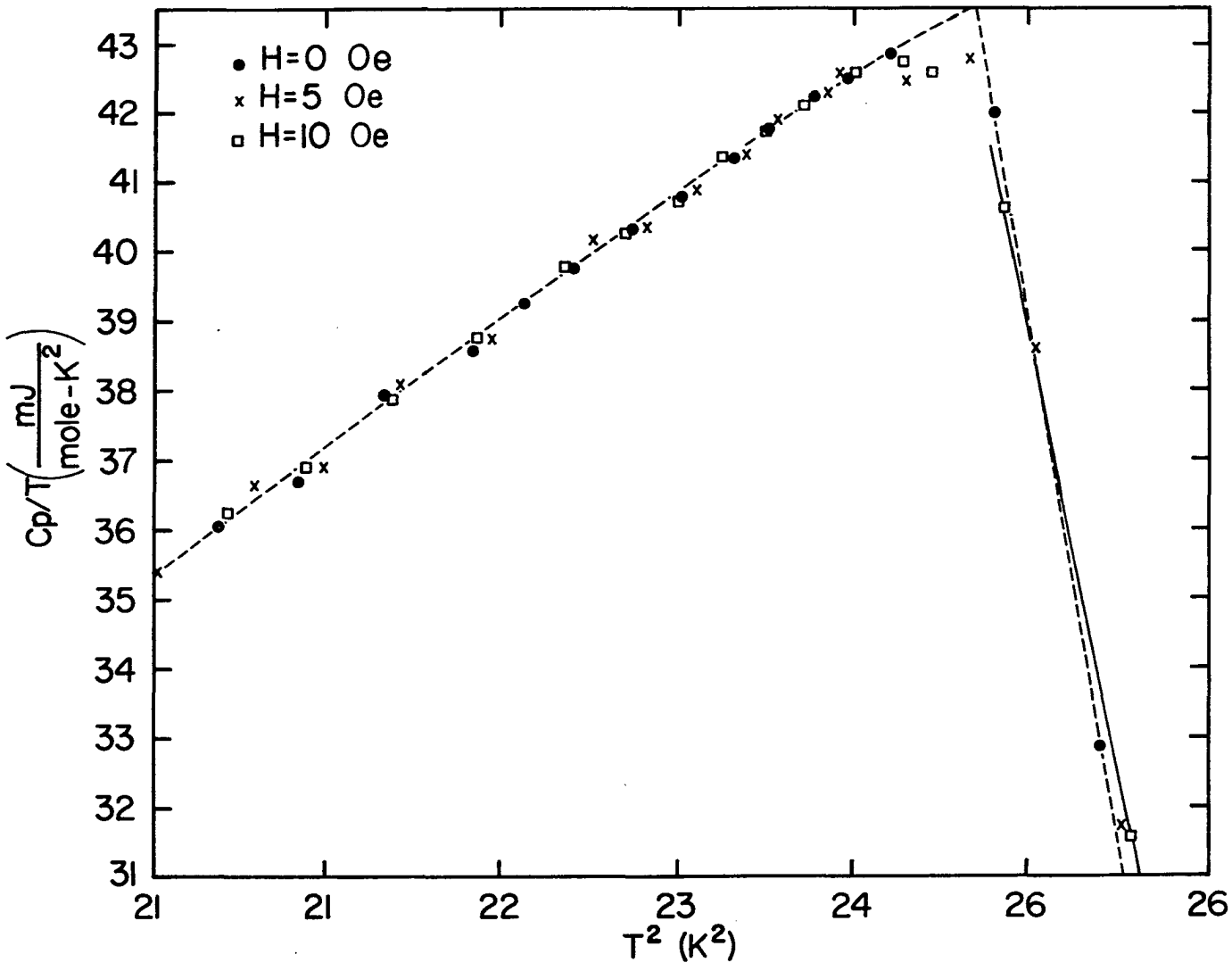

Figure 23. Heat capacity of the ET-2 sample near T = 5 K in a small applied field (C_p/T vs. T^2)

applied field will enter the sample at a field of 0.7 $H_{c1}(0)$, where $H_{c1}(0)$ is the upper critical field at absolute zero. Fig. 24 shows the heat capacities of the ET-2 sample in various applied fields. In this case, all applied fields were perpendicular to the axis of the cylindrical sample, and were kept in the same direction with respect to the sample. The heat capacity at 500 Oe showed one jump and the data in other applied fields showed two or three jumps. Because the first discontinuity, one with the highest transition temperature, jumped up directly from 10 kOe data curve, one would expect that the first jump in the heat capacity in each set of data is due to the normal mixed state superconducting transition. From the value of the applied field and the corresponding temperature at which the first discontinuity occurred, the upper critical field $H_{c2}(T)$ values were obtained and are shown in Fig. 25. By using the least square technique, one finds that the best fit to these values is $H_{c2}(T) = 4869.95 - 6936.99t^2 + 2065.13t^4$, where $H_{c2}(T)$ is in units of Oe. This best fit equation has no physical interpretation but is a convenient way to cast the data. From this best fit equation one obtains $H_{c2}(0) = 4869.95$ Oe for the critical field at absolute zero. When the mean free path $\ell = \infty$ and $K = 2.47$ are assumed, Helfand and Werthamer (44) predicted that $H_{c2}(0) = 3667$ Oe. This value is about 25% lower than the observed value.

From the theory for the type-II superconductor extended by Maki (45), the parameters, K_1, K_2, and K are defined as

$$K_1 = \frac{H_{c2}(T)}{\sqrt{2}\, H_c(T)} \tag{4.4}$$

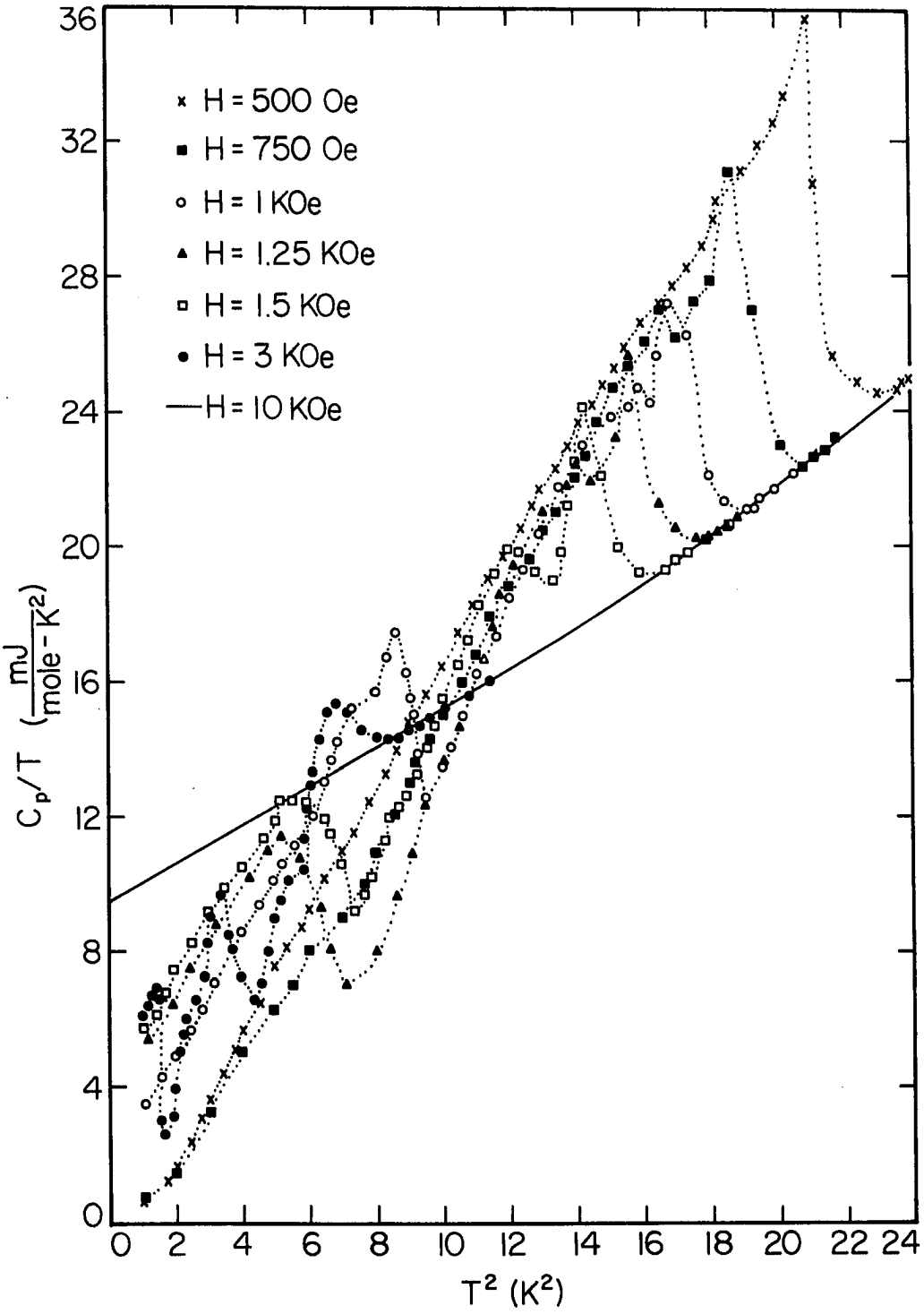

Figure 24. Heat capacity of the ET-2 sample in various applied magnetic field (C_p/T vs. T^2)

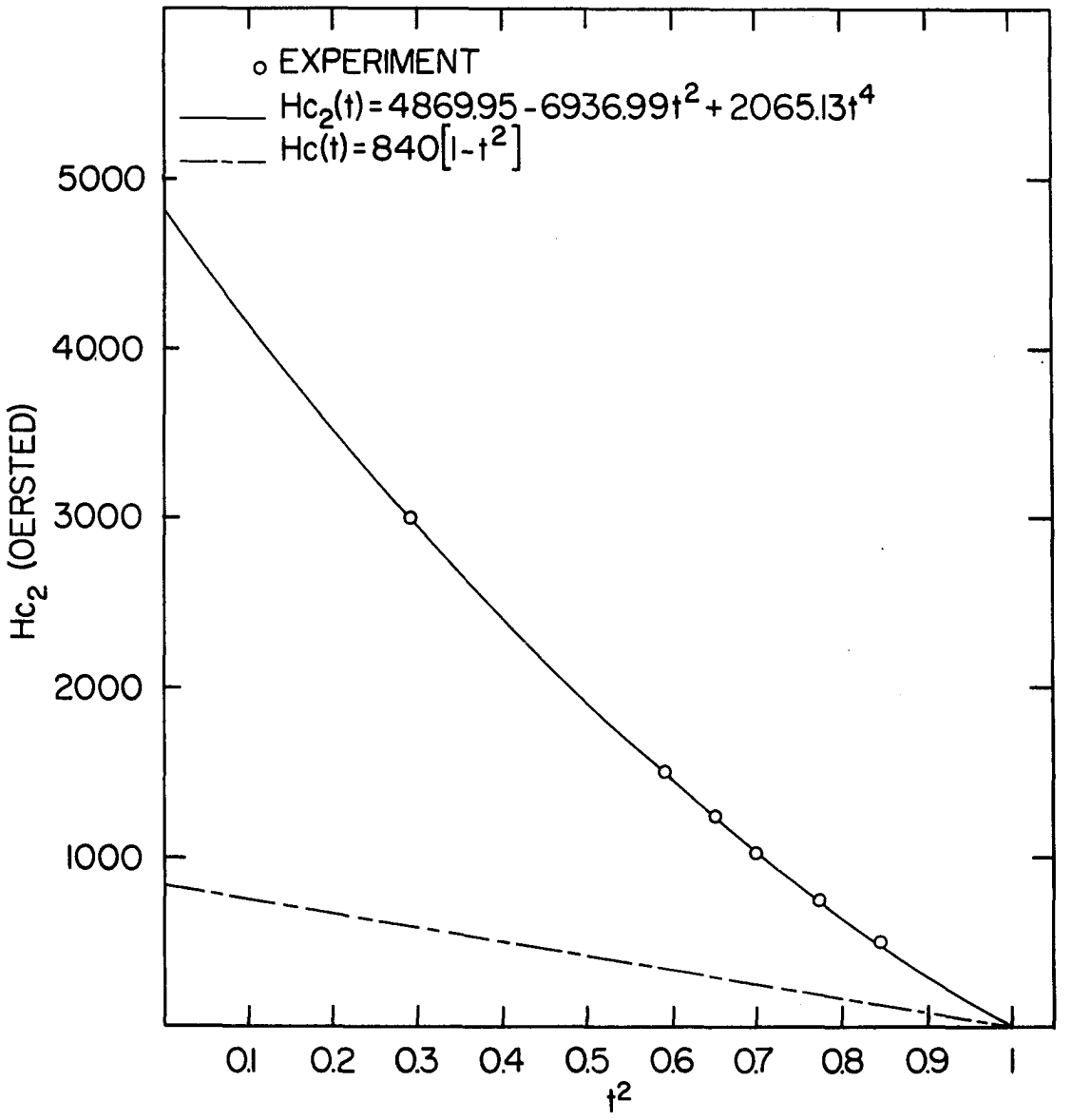

Figure 25. The upper critical H_{c2} of the d-hcp La sample as a function of t^2 where $t = T/T_c$

$$\left(\frac{dM}{dH}\right)_{H_{c2}} = \frac{1}{4\pi\beta_A(2K_2^2 - 1)} \tag{4.5}$$

$$K = K_1(T_c) = K_2(T_c) \ . \tag{4.6}$$

Using Equation (4.4) and the observed values of $H_{c2}(T)$ and $H_c(T)$, the $K_1(T)$ data were obtained and are shown in Fig. 26. By using the least square technique the best fit equation to the K_1 data was found to be $K_1 = 4.136 - 1.832t^2$, and which predicted that the Ginzburg-Landau parameter K is to be 2.3.

According to Goodman (46), the slope of the magnetization curve at $H_{c2}(T_H)$, $(\partial M/\partial H)H_{c2}$, can be obtained from the relation

$$\frac{\Delta C}{VT_H} = \left(\frac{\partial M}{\partial H}\right)_{H_{c2}}\left(\frac{\partial H_{c2}}{\partial T}\right)^2 \ . \tag{4.7}$$

From Equations (4.5) and (4.7), the best fit equation to the H_{c2} data, and the observed values of ΔC and T_H, the values of $K_2(T)$ and $(\partial M/\partial T)H_{c2}$ were obtained and are shown in Table 4. At $T = T_c$, one finds the Ginzburg-Landau parameter K to be 2.47, which is about 7% higher than the value obtained from Equation (4.4). Because the value K = 2.3 was determined only by extrapolating the best fit to the K_1 value o the point $t^2 = 1$, whereas the K_2 values come directly from ΔC data at T_c one may expect that the value K = 2.47 is more reliable. The $K_2(T)$ values are shown in Fig. 26, and the best least square fit equation to the values is found to be $K_2 = 8.487 - 7.365t^2 - 0.728t^4 + 2.074t^6$.

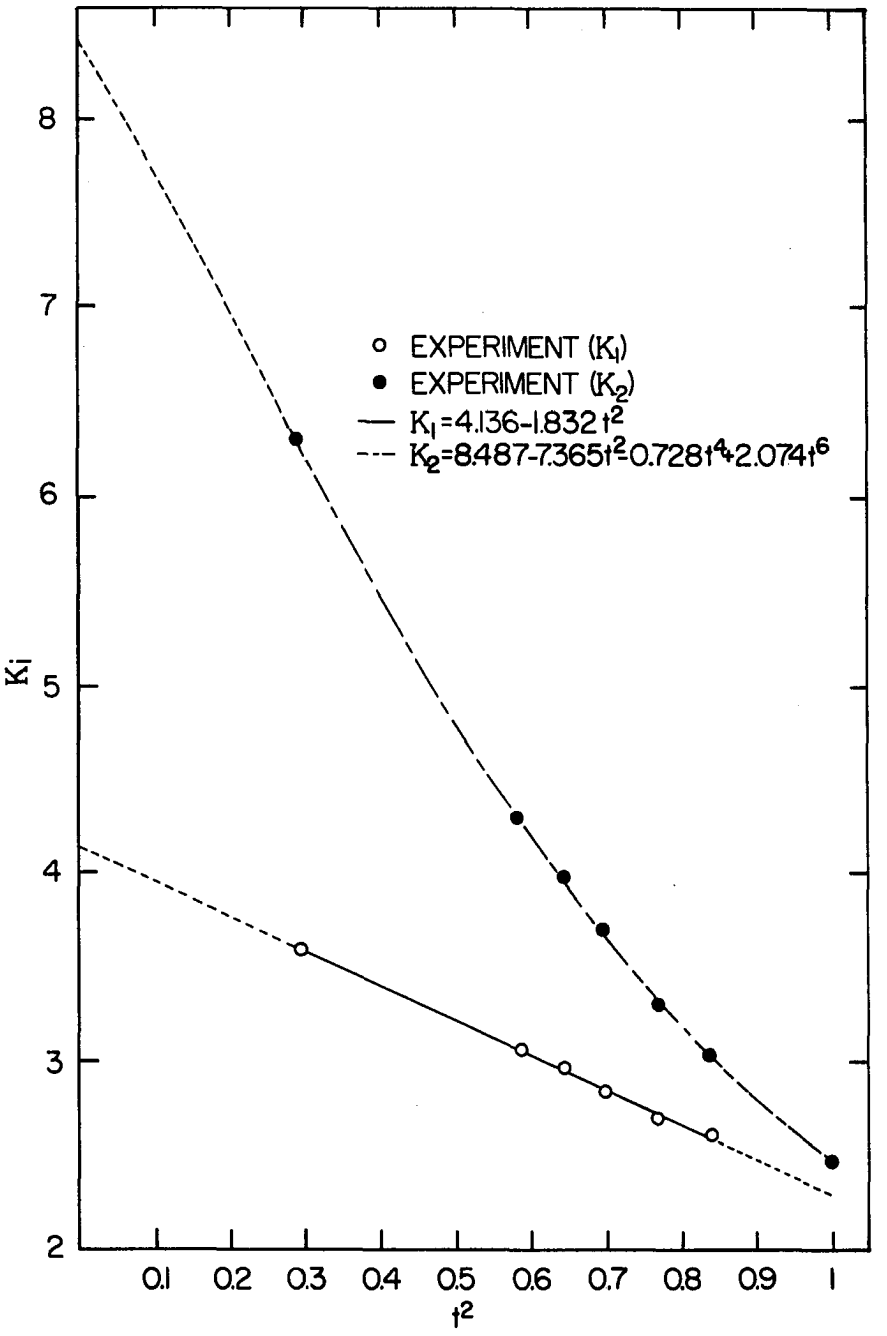

Figure 26. Generalized Ginzburg-Landau parameters, K_1 and K_2, as a function of t^2, where $t = T/T_c$

Table 4. The values of the magnetization data for the ET-2 sample (pure d-hcp La), where $t = T/T_c$ and $T_c = 5.04$ K. K_1 and K_2 are defined in the text

t^2	H_{c2}(Oe)	H_c(Oe)	K_1	K_2	$-(\frac{\partial M}{\partial H})_{H_{c2}}$ $(\frac{G}{Oe})$
1	0	0	2.30	2.47	0.006032
0.839	500	135.7	2.61	3.03	0.003956
0.766	750	195.4	2.71	3.3	0.0034346
0.697	1000	249.0	2.84	3.71	0.002591
0.646	1250	297.6	2.97	3.97	0.0022494
0.589	1500	344.1	3.08	4.33	0.0018864
0.296	3000	591.7	3.59	6.30	0.000875

From the obtained values, the temperature-dependent K_1/K values and K_2/K values were obtained and shown in Fig. 27. The theoretical value of K_1/K predicted by Ginzburg (47), by Bardeen (48), and Gor'kov (49) and by Helfand and Werthamer (44) are also shown in Fig. 27. From this plot, one finds that the observed K_1/K did not follow any theoretical prediction, but the Ginzburg's prediction is the closest one to experiment data. This disagreement of the K_1/K and K_2/K values with theoretical predictions were also found in the experiments for Nb and V. When $K = 2.47$ was used, the value of $[d(K_2/K)]/dt$ at $t^2 = 1$ was found to be -2.09, which is about 12% lower than the value predicted by Maki and Tsuzuki (50). If $K_1(T_c) = 2.47$ was assumed, the new best fit equation to K_1 values provided the value $[d(K_1/K)]/dt = -0.53$ at $t^2 = 1$, which is about 30% higher than the maximum value (-0.41 for

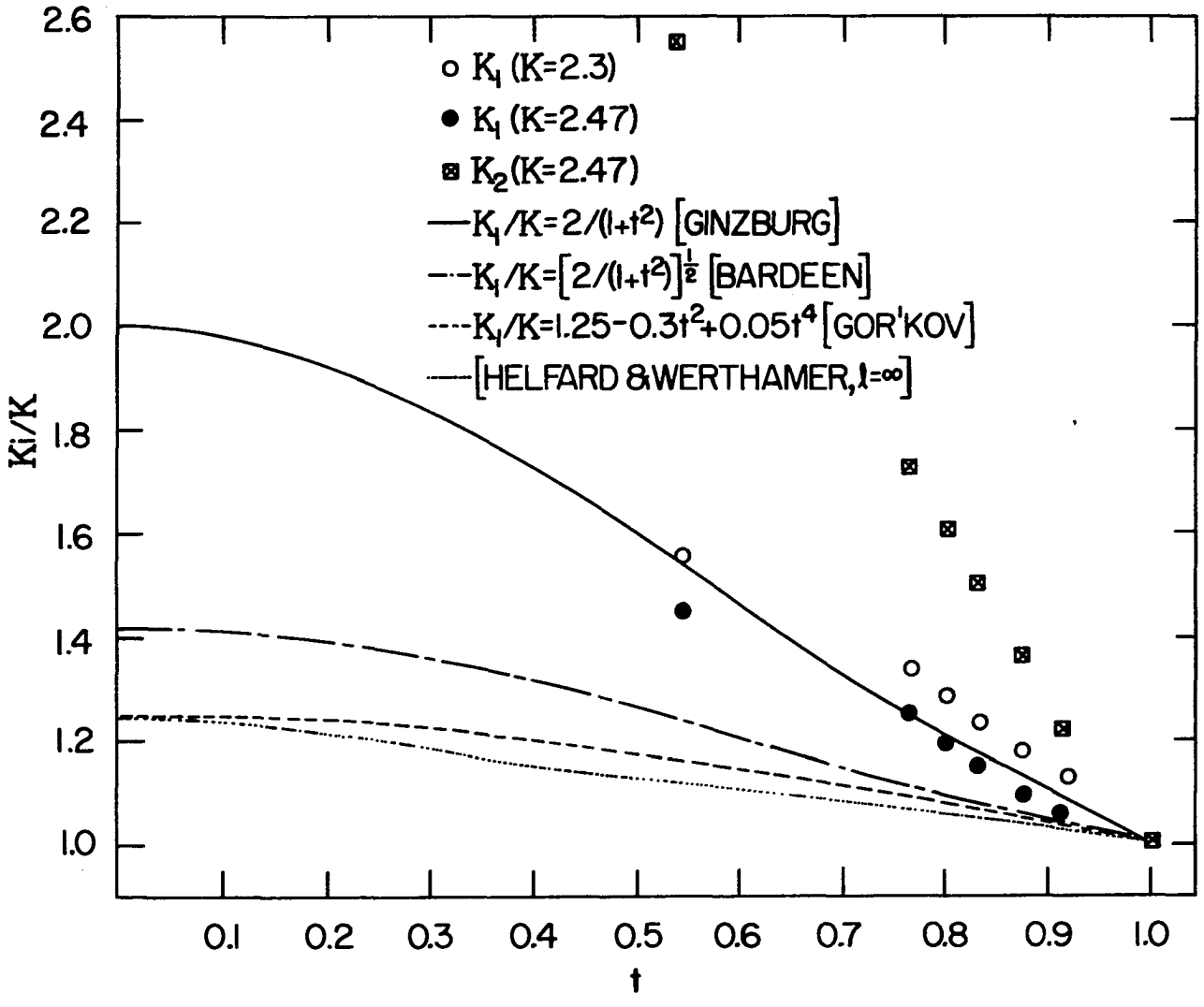

Figure 27. Ratios of K_1/K and K_2/K as a function of the reduced temperature for the pure d-hcp La sample

$\ell = \infty$) predicted by Tewordt (51). These disagreements in both K_1 and K, which were also found in the experimental results for Nb (52) and V (53), reflects the fundamental difficulty in these theoretical treatments.

As reported by Goodman (54), the Ginzburg-Landau parameter K can be expressed as

$$K = K_o + 7.53 \times 10^3 \gamma^{1/2} \rho_o \tag{4.8}$$

where γ is the coefficient of the electronic specific heat in ergs/c.c. $-K^2$ and ρ_o is the normal state resistivity is $\mu\Omega$- cm. For this sample, the ratio $\rho_{300}/\rho_o = 260$, so that $\rho_o = 0.239\mu\Omega$- cm when the average of the ρ_{300} values reported by Legvold et al. (14) = 62.14 $\mu\Omega$- cm was used. From the values of γ and ρ_o, one finds the magnitude of K_o is 2.35, which is much larger than the value $1/\sqrt{2} = 0.71$. This result indicates that the d-hcp La is an intrinsic type II superconductor. Gor'kov (49) suggested that the parameter K_o may be written as

$$K_o = \frac{0.96\lambda_L(0)}{\xi_o} \tag{4.9}$$

and Berlincourt and Hake (55) reported that the intrinsic coherence length ξ_o and the London penetration depth $\lambda_L(0)$ can be determined from the relations

$$\xi_o = \frac{0.18\ k_B S}{12\pi T_c \gamma} \tag{4.10}$$

and

$$\lambda_L(0) = \frac{3h\pi^{1/2}\gamma^{1/2}}{ek_B S} \tag{4.11}$$

where h is the Planck's constant, k_B is the Boltzmann constant, e is the electronic charge in emu, T_c is the transition temperature, γ is the electronic specific heat coefficient in ergs/cm^3 - K^2, and S is the area of the Fermi surface in k- space. Substituting Equation (4.10) and (4.11) into Equation (4.9), the parameter can be expressed as

$$K_o = 1.069 \times 10^3 \left(\frac{h}{ek_B^2}\right)\left(\frac{\gamma^{3/2}T_c}{S^2}\right) . \qquad (4.12)$$

As reported by Fawcett (56), the average Fermi velocity V_F is given by

$$V_F = \frac{k_B^2 S}{6h\gamma} . \qquad (4.13)$$

When the obtained values of γ, T_c, and K_o were used, one finds that $V_F = 0.133 \times 10^8$ cm/sec. from Equation (4.12) and (4.13). Hence, the V_F value for La is a factor of 10 less than that for Cu. Using this V_F value and Equation (4.10) and (4.13), one obtains that $\xi_o = 363$ Å. Substituting this ξ_o value and $K_o = 2.35$ into Equation (4.9), one also obtains $\lambda_L(0) = 888$ Å. Comparing the values of V_F, ξ_o and $\lambda_L(0)$ for La reported here with that for Nb reported by Finnemore et al. (52), one finds the ratios $(V_F)_{La}/(V_F)_{Nb} = 0.44$, $(\xi_o)_{La}/(\xi_o)_{Nb} = 0.85$ and $(\lambda_L(0))_{La}/(\lambda_L(0))_{Nb} = 2.54$, where the subscripts La and Nb indicate the La sample and the Nb sample respectively.

V. DISCUSSION

A. Triclinic Sodium and Lithium Tungsten Oxide Crystals

King et al. (7) have suggested a model in which the lattice heat capacity of hexagonal bronze was composed of Debye lattice heat capacity due to the WO_6 octahedra and an Einstein lattice heat capacity due to the vibration of metal atoms located in the hexagonal holes. To obtain the Einstein contribution, they subtracted the $\gamma T + \beta T^3$ term from the total lattice heat capacity, where β was kept as a constant and was determined from data near 3 K. Bevolo et al. (8) also assumed an Einstein vibration for the excess heat in four hexagonal bronzes, but they obtained the excess heat capacity by subtracting the heat capacity of WO_3 single crystals from the total lattice heat capacity of hexagonal bronze.

From Figures 11 and 12, it is clear that both triclinic crystals show the excess heat with respect to the heat capacity of WO_3 crystals. This behavior is similar to that found in hexagonal bronzes. Therefore, a similar assumption was made that the lattice heat capacity of the triclinic tungsten oxide crystal is due to the vibration of the basic structure - the distorted WO_6 octahedra lattice plus the independent motion of the metal atoms located in the hexagonal holes.

Because the basic cell of WO_3 at low temperature is expected to be a 3-dimension distorted WO_6 octahedra (57), the WO_6 lattice modes of the low-temperature WO_3 shall be very similar to that of the triclinic tungsten oxide crystals. As reported by Bevolo et al. (8), the Debye

temperature of WO_3 at 17 K is 15% smaller than the Debye temperature at 3 K (or at 0 K). This result indicates that the β values of the basic structural lattice of the triclinic samples at 17 K may be probably 45% higher than that at 3 K, so the observed excess heat obtained by the method used by King et al. (7) may be 45% too small at this temperature. In addition, the temperature range, in which the observed excess heat capacity can be fitted well into an Einstein mode, is from 5 K to 50 K for the $Rb_{0.33}WO_3$, $Tl_{0.33}WO_3$ and $Cs_{0.33}WO_3$ crystals reported by Bevolo et al. (8) and is from 5 K to 15 K only for $Rb_{0.33}WO_3$ reported by King et al. (7). Based on the above discussion, the method of finding the excess heat capacity suggested by Bevolo et al. (8) was used in this study.

The Einstein contribution of each sample was obtained by subtracting the lattice heat capacity of WO_3 crystals from the lattice heat capacity of the sample. The Einstein contribution and the best fit equation for $Na_{0.33}WO_3$ and $Li_{0.33}WO_3$ are shown in Fig. 13. The fit of the excess heat capacity to a single Einstein vibration was determined as follows. The Einstein lattice heat capacity is given by

$$C_E = \left(\frac{3R}{4}\right)(S)\left(\frac{T_E}{T}\right)^2 \operatorname{csch}^2\left(\frac{T_E}{2T}\right) \qquad (5.1)$$

where R is the universal gas constant, S is the number of atoms contributing to the heat capacity per formula weight and T_E is the Einstein temperature.

Since there are two unknowns, T_E and S in Equation (5.1), two solutions to the equations are needed. Once two observed excess heat

capacities $C_E(T_1)$ and $C_E(T_2)$ at temperature T_1 and T_2 were substituted into Equation (1) and the expression $C_E(T_2)/C_E(T_1)$ was simplified, a result was obtained

$$\text{Sinh}\left(\frac{T_E}{2T_1}\right) = \left(\frac{T_2}{T_1}\right)\left(\frac{C_E(T_2)}{C_E(T_1)}\right)^{1/2} \text{Sinh}\left(\frac{T_E}{2T_2}\right).$$

Using a hyperbolic identity $\sinh 3\theta = 3 \sinh \theta + 4 \sinh^3\theta$ and taking $T_2 = 3T_1$, Equation (2) reduced to

$$\text{Sinh}\left(\frac{T_E}{2T_2}\right) = \left[\frac{3}{4}\left(\frac{C_E(T_2)}{C_E(T_1)}\right)^{1/2} - 1\right]^{1/2} \tag{5.2}$$

and

$$T_E = 2 \times T_2 \, \text{Sinh}^{-1}\left[\frac{3}{4}\left(\frac{C_E(T_2)}{C_E(T_1)}\right)^{1/2} - 1\right]^{1/2}. \tag{5.3}$$

When the value of T_E was determined from Equation (5.3), it was substituted back into Equation (5.2) to obtain S.

From the values of T_E and S, the excess heat capacity C_E at other temperature was calculated and compared to the observed data. By the same means, other sets of T_E and S values were obtained and tested. The values of T_E and S, which provide an equation with the best fit to the observed excess heat capacity within experimental error are

$T_E = 78 \pm 2$ K, $S = 0.39 \pm 0.03$ for the $Na_{0.33}WO_3$ sample and

$T_E = 71 \pm 2$ K, $S = 0.17 \pm 0.03$ for the $Li_{0.33}WO_3$ sample.

Since the sodium concentration per formula weight ($x = 0.34$) of the sodium tungsten oxide sample agreed with the S value ($S = 0.39$)

obtained from the Einstein excess heat C_E within the experimental errors, the assumption that the excess heat capacity of triclinic tungsten oxide single crystals was due to the vibration of the alkali atoms, was confirmed. Because the observed excess heat can be fitted into one Einstein vibration function within 3% for 15 K < T < 40 K and the ionic radii of Na^+ and Li^+ are small, the alkali ions in the triclinic crystal can be considered as oscillators executing a vibration with the same frequency along x, y and z directions. From the Einstein model discussed in Chapter II, the vibration frequency is given by

$$\nu_E = \frac{k_B T_E}{h} \tag{5.4}$$

where k_B is the Boltzmann constant and h is the Planck's constant. The frequency of a simple harmonic oscillation has

$$\nu = \left(\frac{\pi}{2}\right)\left(\frac{K}{m}\right)^{1/2} \tag{5.5}$$

where κ is the force constant of the restoring force and m is the mass of the oscillator. Solving Equations (5.4) and (5.5), the force constant can be written as

$$\kappa = m\left(\frac{k_B}{h}\right)^2 T_E^{\,2} \tag{5.6}$$

or

$$T_E = \left(\frac{h}{k_B}\right)\left(\frac{K}{m}\right)^{1/2}. \tag{5.7}$$

The force constant obtained from Equation (5.6) for both samples and

the force constants for hexagonal bronzes obtained by Bevolo et al. (8) are shown in Table 5.

Table 5. Einstein temperature T_E and related data for the triclinic sodium and lithium tungsten oxide samples, and three hexagonal bronzes[a]

	$Na_{0.33}WO_3$	$Li_{0.33}WO_3$	Rb_xWO_3	Cs_xWO_3	Tl_xWO_3
T_E(K)	78±2	71±2	58±2	70±2	38±3
S	0.39±0.03	0.17±0.02	0.29±0.02	0.32±0.02	0.33±0.02
m (amu)	23	7	86	133	204
κ $(\frac{N}{m})$	4	1	8	19	8
RR[b]	0.5	0.36	0.75	0.83	0.75

[a]The data for Rb, Cs and Tl hexagonal bronzes were reported by Bevolo et al. (8).

[b]The radii ratio, RR, is defined as a ratio of the ionic radii to the cavity.

Because the volumes of the reduced cell of $Na_{0.33}WO_3$ and $Li_{0.33}WO_3$ changes only slightly, the size of the hexagonal holes available for locating the metal atoms are nearly the same. The restoring force acting on the metal atoms, which was dominated by the coupling due to the orbital overlap between the alkali atoms and the nearest oxygen atoms, will depend on the size of the metal atoms. A metal atom with larger ionic radii will experience a larger restoring force and would have a larger force constant. The conclusion explains the result that

the force constant of $Na_{0.33}WO_3$ ($\kappa = 4\frac{N}{m}$) is larger than that of $Li_{0.33}WO_3$ ($\kappa = 1\ \frac{N}{m}$). Equation (5.7) predicts a smaller T_E for a heavier ion with the same κ. Therefore, the larger the M^+ ion, the greater the force constant, also helps to account for the result that the heavier Na^+ ion has a larger T_E (see Table 5).

Jamieson et al. (58) suggested that the Li^+ ion in $K_{1-x}Li_xNbO_3$ which has a tetragonal bronze structure were located in the triangular holes instead of in the bigger tetragonal holes. Granham and Wadsley (59) found that it is not structurally necessary to have actions located in the hexagonal channel of $MoW_{11}O_{36}$ and $MoW_{14}O_{45}$, which have hexagonal bronze structure. Based on the experimental results for the $Li_{0.33}WO_3$ sample, it may be possible that there exists a second type of hole which is large enough to be occupied by a Li^+ ion but too small for the Na^+ ion. Furthermore, the radii of this small cavity would be small enough that the Li^+ ions would be strongly coupled to nearest neighbors. Under this assumption, some of the Li^+ ions in $Li_{0.33}WO_3$ would be located in the small holes and would not contribute an Einstein mode. This would account for the result that the S value (S = 0.17) obtained from the excess heat capacity is smaller than the lithium concentration of the $Li_{0.33}WO_3$ sample (x = 0.33). Since the S value for the $Li_{0.33}WO_3$ sample is 0.17, about 50% (0.16/0.33) of Li^+ ions of the $Li_{0.33}WO_3$ sample are strongly coupled to their neighbors. The evidence of a stronger coupling with a larger Debye temperature helps to explain the result that the Debye temperature of $Li_{0.33}WO_3$ (θ_D = 341 K) is larger than that of $Na_{0.33}WO_3$ (θ_D = 279 K) in spite of the fact that the

radii of the Li^+ ion (0.68 Å) is smaller than that of the Na^+ ion (0.95 Å).

For both triclinic tungsten oxide samples, the Einstein temperatures T_E are larger than for the hexagonal bronzes (see Table 5), but the force constants are smaller than the force constant found in hexagonal bronzes. Since the radii ratio, which is defined as the ratio of the radii of the metal ion to the radii of the hexagonal cavity, is 0.36 for $Li_{0.33}WO_3$, 0.5 for $Na_{0.33}WO_3$, 0.75 for Rb_xWO_3 and 0.83 for Cs_xWO_3, the evidence that a smaller radii ratio provides a smaller restoring force predicts the result that $\kappa_{Li} = 1 < \kappa_{Na} = 4 < \kappa_{Rb} = 8 < \kappa_{Cs} = 19$, where κ_M is the force constant of the $M_{0.33}WO_3$ crystal and is in the units of $\frac{N}{m}$.

Within experimental error, only a single characteristic temperature T_E was found for both triclinic samples. This result is the same as that found by Bevolo et al. (8) for Rb, Tl, and Cs hexagonal bronzes and that found by King et al. (7) for $Rb_{0.33}WO_3$. This is to be contrasted with the result of the low-temperature Mossbauer spectra reported by McColm et al. (60) for hexagonal Sn_xWO_3, which showed an anisotropy for hexagonal Sn_xWO_3. Because the heat capacity measurements are an average over many microscopic properties, the Einstein temperature T_E reported here is an average over all directions.

As shown in Fig. 13, the observed excess heat capacity for $Na_{0.33}WO_3$ is higher than the values given by the best fit equation for temperatures below 12 K. The same behavior occurs for the $Li_{0.33}WO_3$ sample for T < 8 K. The fact that the Debye temperature of WO_3 (380 K) (8)

is higher than that of triclinic crystals, suggested that at lower temperatures the WO_6 lattice heat capacity for WO_3 crystals is smaller than that for triclinic phases. This suggestion helps to account for the higher observed excess heat capacities for both samples at lower temperature. At higher temperature, the WO_3 lattice contribution is larger, the errors in the excess heat capacity increase from 4% at lower temperature to 8% at 60 K. For $T > 50$ K, the excess heat capacities for both triclinic samples show a systematic low deviation from the best fit curve. Because this systematic low deviation at higher temperature also occurred at the excess heat capacity of the hexagonal bronzes reported by Bevolo et al. (8), one may expect that the assumption of having the same Debye lattice heat capacity for the WO_3 crystal and the triclinic crystals is not reliable at higher temperatures.

For the triclinic crystals, the presence of more than one Einstein vibration of the M^+ ion may be the cause of the deviation of the observed excess heat capacity from the best fit equation at lower and higher temperatures, but at present the real cause in not understood.

B. Lanthanum

From Table 6, one finds that the values of γ and θ_D reported here are different from those reported by Johnson and Finnemore (JF) (19) by approximately 2%. The presence of different amounts of the gas impurities in those samples (see Table 2), or the uncertainty of determining the percent of the α and β phase in each sample might cause this difference in the γ and θ_D values.

Table 6. The parameters in the normal state and in the superconducting state for the pure d-hcp La reported here and that reported by Johnson and Finnemore (19)

	Present work	JF data[a]
T_c(k)	5.04±0.01	4.87±0.02
ΔT_c(k)	0.104±0.01	0.2
ΔC(mJ/mole-k)	85±2	78.5±4
γ(mJ/mole-k)	9.45±0.02	9.4±0.1
θ_D(k)	150±1.0	152±1.5
$(\theta_D)_{min}$(k)	11.1±0.1	--[b]
T_c/θ_D	0.034±0.001	0.032±0.001
$\Delta C/\gamma T_c$	1.78±0.08	1.71±0.11
V(cm^3/mole)	22.54±0.04	22.54±0.04
$H_c(0)$ (OERSTED)	840±10	798±12
$2\Delta(0)/k_BT_c=[2\pi VH_c(0)/3\gamma T_c]^{\frac{1}{2}}$	3.73±0.2	3.67±0.22
$N(0)V=1/[\ell n(1.14x\theta_D/T_c)]$	0.284	0.280
V_p(ev)	0.143±0.015	0.140±0.02
K_o	2.47	--
$H_{c2}(0)$ (OERSTED)	4869.9±10	--
$H_{c1}(0)$[c] (OERSTED)	372.5±10	--

[a]Corrected data for pure d-hcp La reported by Johnson and Finnemore (19).

[b]Not determined.

[c]Obtained from the relation $H_{c1}=H_c(K\sqrt{2})^{0.65}$ suggested by Goodman (61).

Comparing the values of T_c and ΔT_c of the ET-2 sample with that of the ET-1 sample and the sample reported by Finnemore et al. (22), one finds that the T_c value increases and the ΔT_c value decreases with increasing purity of phase homogenity. These results agree with the empirical evidence that the single-crystal sample has narrow transition width than the polycrystalline sample, and that the T_c decreases with increasing impurities.

The present work on the jump in the heat capacity at T_c, on the value of the energy gap and on the deviation function of the critical field D(t) shows a small but easily measured disagreement with BCS prediction. This disagreement is not surprising when one realizes that BCS were made under the weak-coupling assumption, i.e. the value of T_c/θ_D is the order of 0.0033 or less. As expected from an intermediate coupling superconductor, the T_c/θ_D value reaches about 0.033, e.g. 0.031 for In and 0.037 for Bn, the $\Delta C/\gamma T_c$ value increases to about 1.7 and the energy gap value increases to about 3.7. Furthermore, the deviation function D(t) of the materials with T_c/θ_D being about 0.033 lie between the weak-coupling curve, as in the case for Sn and the strong-coupling curve, as in the case for Hg. From the deviation function of La shown in Fig. 22, and the values of T_c/θ_D and $2\Delta(0)/k_BT_c$ for different materials shown in Table 7, one might classify La as an intermediate coupling superconductor.

From Table 6, one also finds that the value of the energy gap $2\Delta(0)/k_BT_c$ reported here is slightly higher than that reported by JF. Because the ET-2 sample has high purity, the presence of the energy gap

Table 7. The values of T_c/θ_D, and $2\Delta(0)/k_BT_c$ for various metals[a]

Metals	T_c/θ_D	$2\Delta(0)/k_BT_c$
Al	0.003	3.2
BCS	0	3.53
Sn	0.019	3.60
In	0.031	3.64
La[b]	0.034	3.73
Nb	0.037	3.66
Hg	0.052	3.96

[a]Data from report of Finnemore et al. (52) except that for La.

[b]Data for pure d-hcp La reported here.

anisotropy or the absence of the impurity state in the gap shall be the cause of the larger energy gap value. When one considers that the D(t) curve for the ET-2 sample is closer to the D(t) curve of the Hg sample than the JF data curve does, one might expect that the superconducting coupling for the ET-2 sample is stronger than the JF sample. This suggestion helps to account for the result that the value of $\Delta C/\gamma T_c$ and V_p for the pure d-hcp La reported here is larger than that reported by JF.

As shown in Fig. 22, one finds that the slope of the $\ell n(C_{es}/\gamma T_c)$ vs. T/T_c data curve for the CE-2 sample change significantly with increasing T_c/T. This result is expected, if the energy gap anisotropy

is present in this sample. The comparisons of the BCS data with the ET-2 data and with the JF data at the lower temperatures clearly reveal that the ET-2 data show more upward deviation from the BCS prediction than the JF data do. The result that a sample with higher purity show a greater deviation indicates that this upward deviation at the lower temperature is due to the energy gap anisotropy or the impurity state in the gap. At temperature near T_c, the ET-2 data rise above the theoretical curve again and reach a value $\Delta C/\gamma T_c = 1.78$. The deviation at $T_c/T \sim 1$ is believed to be a characteristic of an intermediate or strong coupling superconductor. Also from Fig. 22, it is clear that the ET-2 data is very similar to the JF data and also in good agreement with the law of corresponding states.

Using the BCS prediction of $\Delta C \sim (\Delta(0)/k_B T_c)^2$, one finds that the value of ΔC for the ET-2 sample in $\Delta C = 1.43\gamma T_c \times (3.73/3.52)^2 = 1.6\gamma T_c$. From this result, one might expect that the ΔC value of the ET-2 sample goes to $1.6\gamma T_c$ due to the increase of the energy gap value, and the rest is due to the energy gap anisotropy.

From the classical calculations by Peierls (62), the jump in the heat capacity of a type-I superconductor in a small applied field H should show a large sharp peak near the transition temperature. This transition with a latent heat has been confirmed by many experimental results (63). Comparing the Peierls' calculation with the data shown in Fig. 23, it is clear that the superconducting transition in a small applied magnetic field for the ET-2 sample is a second order transition. This evidence, as well as the fact that a high magnetic field is

necessary ($H > 3$ kOe) for completely suppressing the superconductivity of this sample, strongly suggested that this d-hcp is a type-II superconductor.

As shown in Fig. 20, one finds that the second and the third jumps of heat capacity increase as the applied magnetic field increases. This result suggested that the second and the third discontinuity is not due to the presence of a small amount of the fcc La. Because the total magnetic impurities in the ET-2 sample are less than 100 atomic ppm, and the second and the third jumps in the heat capacity occurred only down to 5 K, one can expect that these discontinuities are not due to the presence of the magnetic impurities. If one assumed that the second or third discontinuity is the result of the mixed $\leftrightarrow$ Meissner phase transition, then the thermodynamic critical field at $T = 0$ K should be larger than 3 kOe. When $H_c(0) = 3$ kOe is assumed, one finds from Equation (4.8) that the new entropy difference should be at least 12 times larger than the experimental entropy difference. Unfortunately, a value 12 times the experimental entropy difference is at least 2 times larger than the experimental total entropy in the normal or superconducting state. This discussion shows that the mixed $\leftrightarrow$ Meissner phase transition is not the real cause of these discontinuities in the heat capacity. The geometric effect might be the cause of these second and third jumps of heat capacity, but at present the real cause is unknown.

From Fig. 26, it is clear that the K_2 values exceed the K_1 values for temperatures below T_c, and the K_2 value increases more rapidly than the K_1 value with decreasing temperature. These results agree with the

relationship, $K_2 > K_1 > K$, for an intrinsic type-II superconductor predicted by Maki and Tsuzuki (50) with the experimental result of $K_2 \simeq K_1$ for the dirty superconductor reported by McConville and Serin (64) and Mardion et al. (65).

VI. CONCLUSIONS

A. Triclinic Sodium and Lithium Tungsten Oxide Crystals

This experiment clearly shows that an excess heat capacity is present in both the sodium and lithium tungsten oxide samples. By assuming that the heat capacity of the basic lattice structure is the same for the triclinic crystals and WO_3, the excess heat capacity for each triclinic crystal has been analyzed and found to be contributed by a single Einstein vibration of the M^+ ion located in the hexagonal holes. The relation between the Einstein temperature and the mass and ionic radii of the M^+ ion has also been analyzed semiquantitatively. Because the heat capacity measurements provide an average over many properties of the materials, no significant difference has been found between the vibration of the M^+ ion located in the hole without a hexagonal channel and that with hexagonal channels. The phonon density of state and some other properties of these triclinic crystals should show the characteristics of the Einstein phonon mode.

B. Lanthanum

In the normal state, this work gives $\gamma = 9.45(\text{mJ/mole-k}^2)$, $\theta_D = 150$ K and the minimum of $\theta_D = 11.1$ K for the high purity single d-hcp La. In the superconducting state, this experiment has shown that the d-hcp La, like niobium and vanadium, is an intrinsic type-II superconductor. From the zero-field superconducting data, the d-hcp La has been shown to be an intermediate-coupling superconductor with the deviation function of the critical field midway between mercury and tin.

Also from the zero-field superconducting data, the d-hcp La has been shown to obey the law of corresponding states quite well. The disagreement of the values of K_1/K and K_2/K with the theoretical prediction, which also were found in the results for Nb and V, indicates the fundamental difficulty in applying the GLAG theory and its extension to the intrinsic type-II superconductors.

VII. BIBLIOGRAPHY

1. A. Magnéli, Nature 169, 791 (1952).

2. H. R. Shanks, J. Cryst. Growth 13/14, 433 (1972).

3. H. F. Franzen, H. R. Shanks and B. H. W. S. de Jong, National Bureau of Standards Special Publication 364, Solid State Chemistry, Proceedings of 5th Materials Research Symposium (1972).

4. R. W. Vest, M. Griffel and J. F. Smith, J. Chem. Phys. 28, 293 (1958).

5. B. C. Gerstein, A. H. Klein and H. R. Shanks, J. Phys. Chem. Solids 25, 177 (1964).

6. W. E. Kienzle, A. J. Bevolo, G. C. Danielson, P. W. Li, H. R. Shanks and P. H. Sidles, in Proceedings of the Thirteenth International Conference on Low Temperature Physics, Boulder, Colorado, 1972, edited by R. H. Kropschot and K. D. Timmerhaus (University of Colorado Press, Boulder, Colorado, 1973).

7. C. N. King, T. A. Benda, W. A. Phillips and T. H. Geballe, in Proceedings of the Thirteenth International Conference on Low Temperature Physics, Boulder, Colorado, 1972, edited by R. H. Kropshot and K. D. Timmerhaus (University of Colorado Press, Boulder, Colorado, 1973).

8. A. J. Bevolo, H. R. Shanks, P. H. Sidles and G. C. Danielson, Phys. Rev. 9, 3220 (1974).

9. K. Mendelssohn and J. G. Daunt, Nature 1, 473 (1937).

10. W. T. Ziegler, J. E. Young and R. Eloyd, J. Am. Chem. Soc. 75, 1215 (1953).

11. W. T. Ziegler and F. H. Horn, J. Chem. Phys. 16, 838 (1948).

12. G. S. Anderson, S. Legvold and F. H. Spedding, Phys. Rev. 109, 243 (1958).

13. N. R. James, S. Legvold and F. H. Spedding, Phys. Rev. 88, 1092 (1952).

14. S. Legvold, P. Burgardt, B. J. Beaudry and K. A. Gschneidner, Jr., Phys. Rev. 16, 2479 (1977).

15. J. D. Leslie, R. L. Cappelletti, D. M. Ginsberg, D. K. Finnemore, F. H. Spedding and B. J. Beaudry, Phys. Rev. 134, A309 (1964).

16. A. S. Edelstein and A. M. Toxen, Phys. Rev. Lett. 17, 196 (1966).

17. J. J. Hauser, Phys. Rev. Lett. 179, 921 (1966).

18. H. J. Levinstein, V. G. Chirba and J. E. Kunzler, Phys. Lett. 24A, 362 (1967).

19. D. L. Johnson and D. K. Finnemore, Phys. Rev. 158, 376 (1967).

20. D. H. Parkinson, F. E. Simmon and F. H. Spedding, Proc. Roy. Soc. (London) A207, 137 (1951).

21. A. Berman, M. W. Zemansky and H. A. Boorse, Phys. Rev. 109, 70 (1958).

22. D. K. Finnemore, D. L. Johnson, J. E. Ostenson, F. H. Spedding and B. J. Beaudry, Phys. Rev. 137, A550 (1965).

23. R. G. Jordon, D. W. Jones and P. G. Mattocks, J. Less-Common Metals 31, 125 (1974).

24. As described by E. S. Gopal, Specific heat at low temperatures (Plenum Press, New York, 1966), p. 25.

25. P. Debye, Ann. Physik 39, 789 (1912).

26. J. Bardeen, L. N. Copper and J. R. Schrieffer, Phys. Rev. 108, 1175 (1957).

27. D. Shoenberg, Superconductivity (Cambridge University Press, Cambridge, England, 1965), 2nd ed.

28. B. S. Chandrasekhar, and J. A. Rayne, Phys. Rev. Lett. 6, 3 (1961).

29. P. G. de Gennes, Superconductivity of Metals and Alloys (Benjamin, New York, 1966).

30. A. A. Abrikosov, Soviet Phys. JETP 5, 1174 (1957).

31. B. B. Goodman, Phys. Lett. 12, 6 (1964).

32. C. A. Swenson, Metrologia 9, 99 (1973).

33. W. R. Dekker and D. K. Finnemore, Phys. Rev. 172, 430 (1968).

34. A. J. Bevolo, H. R. Shanks and D. E. Eckels, Phys. Rev. 13, 3522 (1976).

35. H. R. Shanks, Ames Laboratory-DOE, Ames, Iowa, private communication.

36. B. H. W. S. de Jong, M.S. thesis, Iowa State University, 1971 (unpublished).

37. B. J. Beaudry and K. A. Gschneidner, Jr., Preparation and Basic Properties of the Rare Earth Metals, Chapter 2 of Handbook on the Physics and Chemistry of Rare Earths, edited by K. A. Gschneidner, Jr. and L. Eyring (North-Holland Publishing Co., Amsterdam).

38. G. T. Furukawa, W. G. Saba and M. L. Reilly, Natl. Stand. Ref. Data Ser. 18, 1 (1968).

39. J. C. Holste, T. C. Cetas, and C. A. Swenson, Rev. Sci. Instrum. 43, 670 (1972).

40. M. Blackman, Proc. Roy. Soc. A148, 365 (1945).

41. D. K. Finnemore and D. E. Mapother, Phys. Rev. 140, A507 (1965).

42. K. A. Gschneidner, Jr., Rare Earth Alloys (D. Van Nostrand, Inc., Princeton, New Jersey, 1064).

43. B. B. Goodman, Compt. Rend. 246, 3031 (1958).

44. E. Helfand and N. R. Werthamer, Phys. Rev. Lett. 13, 686 (1964); Phys. Rev. 147, 288 (1966).

45. K. Maki, Physics 1, 21 (1964).

46. B. B. Goodman, Phys. Lett. 1, 215 (1962).

47. V. L. Ginzburg, Soviet Phys. JETP 3, 621 (1956).

48. J. Bardeen, Phys. Rev. 94, 554 (1954).

49. L. P. Gor'kov, Soviet Phys. JETP 10, 593 (1960).

50. K. Maki and T. Tsuzuki, Phys. Rev. 139, A868 (1965).

51. L. Tewordt, Z. Physik 184, 319 (1965).

52. D. K. Finnemore, T. F. Stromberg, and C. A. Swenson, Phys. Rev. 149, 231 (1966).

53. R. Radebaugh and P. H. Keesom, Phys. Rev. 149, 217 (1966).

54. B. B. Goodman, IBM J. Res. Develop. 147, 288 (1962).

55. T. G. Berlincourt and R. R. Hake, Phys. Rev. 131, 140 (1963).

56. E. Fawcett, J. Phys. Chem. Solids 18, 320 (1961).

57. S. Tanisaki, J. Phys. Soc. Jap. 15, 566 (1960).

58. P. B. Jamieson, S. C. Abrahams, and J. L. Bernstein, American Crytal. Assoc. Meeting, Minneapolis, August 1967.

59. J. Granham and A. D. Wadsley, Acta Cryst. 14, 379 (1961).

60. J. McColm, R. Steadman, and A. Howe, J. Solid State Chem. 2, 555 (1970).

61. B. B. Goodman, I.B.M. J. Res. Develop. 6, 63 (1962).

62. R. Peierls, Proc. Roy. Soc. A155, 613 (1936).

63. D. C. Rorer, D. G. Onn, and H. Meyer, Phys. Rev. 138, A1661 (1965).

64. T. McConville and B. Serin, Phys. Rev. 140, A1169 (1965).

65. G. B. Mardion, B. B. Goodman, and A. Lacaze, J. Phys. Chem. Solids 26, 1143 (1965).

VIII. ACKNOWLEDGEMENTS

I wish to thank my major professor, Dr. G. C. Danielson for his encouragement, guidance and assistance during this research. I also wish to thank Dr. D. K. Finnemore and H. R. Shanks for reading and constructive criticism of this thesis in Dr. Danielson's absence. I wish to thank D. K. Finnemore, Dr. A. J. Bevolo, H. R. Shanks and Dr. S. H. Liu for their many helpful discussions. I wish to thank Dr. D. K. Finnemore for helping me to determine the resistivity ratio of the La sample. I thank Dr. A. J. Bevolo for teaching me the fundamentals of the low-temperature heat capacity measurement. I wish to thank H. R. Shanks for his skillful preparation of the triclinic sodium and lithium tungsten oxide samples. I also with to thank B. J. Beaudry and F. A. Schmidt for their skillful preparation and purification of the La samples. I thank O. M. Sevde for many technical assistances.

I wish to thank my wife, Fei-Wei, for her love, understanding and assistance, which permitted me to pursue this research.

IX. APPENDIX A: HEAT CAPACITY OF ASRC COPPER FROM 1 K TO 60 K, WHERE T IS IN KELVIN, C IN mJ/mole-K AND H IN OERSTED

H = 0		T	C	T	C	T	C
T	C	3.933	5.620	16.08	228.1	33.11	2266.8
		4.033	5.906	16.57	250.9	34.26	2487.9
1.001	0.733	4.369	6.994	17.12	279.1	35.08	2646.8
1.154	0.864	4.514	7.494	17.82	316.7	36.38	2914.6
1.217	0.919	4.764	8.443	18.66	367.7	37.31	3135.3
1.351	1.062	4.950	9.169	19.09	397.0	38.27	3350.8
1.485	1.191	5.252	10.51	19.59	431.0	39.44	3629.5
1.503	1.290	5.636	12.42	20.10	470.4	40.59	3885.5
1.621	1.319	5.901	13.87	20.66	513.3	41.20	4024.4
1.736	1.441	6.359	16.63	21.24	563.1	42.49	4344.7
1.843	1.583	6.763	19.44	21.87	618.8	43.17	4508.7
1.986	1.730	7.074	21.83	22.59	689.3	44.55	4856.9
2.037	1.812	7.484	25.17	23.36	768.4	45.33	5009.8
2.122	1.924	8.075	30.79	24.19	859.2	46.19	5260.0
2.247	2.093	8.451	34.79	25.10	969.8	47.03	5429.9
2.332	2.216	9.096	42.57	25.65	1037.8	48.89	5896.0
2.415	2.340	9.526	48.43	26.32	1124.9	49.89	6144.7
2.509	2.486	10.07	56.57	26.99	1216.1	50.89	6438.3
2.614	2.656	10.83	69.51	27.46	1286.3	52.00	6727.5
2.722	2.841	11.54	83.57	27.96	1361.6	53.14	6945.2
2.854	3.077	12.08	95.51	28.45	1434.8	54.33	7235.5
2.944	3.247	12.78	112.9	29.01	1519.3	55.59	7558.7
3.011	3.380	13.28	126.4	29.56	1611.9	56.93	7940.7
3.246	3.867	13.83	143.1	30.44	1764.5	58.37	8236.6
3.568	4.623	14.48	164.4	31.06	1874.8	59.88	8649.6
3.734	5.051	15.20	191.2	32.04	2043.5		

X. APPENDIX B: HEAT CAPACITY OF SODIUM TUNGSTEN OXIDE SAMPLE FROM 1 K TO 60 K, WHERE T IS IN KELVIN, C IN mJ/mole-K AND H IN OERSTED

H = 0		T	C	T	C	T	C
T	C	2.782	8.402	14.53	1593.4	38.17	12008.8
		2.844	8.931	15.38	1865.5	39.21	12554.9
1.027	0.452	2.910	9.575	15.90	2037.8	40.49	13184.4
1.105	0.514	2.987	10.33	16.88	2394.1	41.10	13397.8
1.204	0.680	3.003	10.57	17.75	2723.9	42.29	14010.0
1.300	0.858	3.157	12.27	18.70	3104.9	43.73	14690.2
1.389	1.069	3.340	14.56	20.92	3995.3	44.49	14984.2
1.476	1.270	3.772	21.31	21.46	4189.3	45.94	15748.0
1.539	1.400	4.019	25.76	22.04	4433.2	46.76	15975.1
1.616	1.632	4.317	32.18	23.31	4988.1	47.63	16347.5
1.709	2.016	4.724	42.99	24.06	5400.3	48.34	16717.1
1.783	2.265	5.133	56.57	25.67	6124.7	49.08	17109.4
1.887	2.604	5.645	77.42	26.63	6578.3	50.90	17814.3
1.954	2.893	6.217	101.3	27.74	7091.1	51.96	18417.5
2.064	3.385	6.727	134.9	28.99	7679.6	53.06	18895.3
2.156	3.882	7.711	220.5	30.32	8335.3	54.26	19461.3
2.220	4.308	8.576	317.3	31.76	9059.4	55.38	19856.1
2.304	4.816	9.047	379.5	33.42	9805.6	56.69	20504.2
2.394	5.338	9.905	509.1	34.61	10333.4	58.17	21141.2
2.490	5.976	10.85	671.8	35.38	10763.1	59.72	21908.1
2.573	6.587	11.67	841.5	36.01	10985.9		
2.651	7.238	12.83	1115.2	36.53	11309.6		
2.715	7.846	13.72	1352.3	37.60	11650.4		

XI. APPENDIX C: HEAT CAPACITY OF LITHIUM TUNGSTEN OXIDE SAMPLE FROM 1 K TO 60 K, WHERE T IS IN KELVIN, C IN mJ/mole-K AND H IN OERSTED

H = 0		T	C	T	C	T	C
T	C	2.809	5.879	16.69	1739.5	39.48	10257.4
		2.916	6.443	17.72	2038.2	40.85	10851.7
1.012	0.623	2.983	6.862	18.43	2250.7	41.77	11264.0
1.089	0.675	3.147	7.962	19.38	2563.8	42.63	11564.5
1.208	0.874	3.254	8.688	20.51	2933.2	43.55	11908.2
1.277	0.945	3.445	9.680	21.44	3263.6	44.37	12237.1
1.345	1.052	3.831	13.52	22.33	3572.3	45.62	12774.9
1.390	1.212	4.202	17.31	23.51	3988.6	46.39	13141.5
1.487	1.300	4.613	22.86	24.48	4344.8	47.52	13642.8
1.552	1.428	5.032	29.69	25.55	4726.7	48.45	14007.8
1.654	1.643	5.774	46.45	26.68	5145.4	49.21	14292.5
1.739	1.712	6.375	78.41	27.45	5423.9	50.67	14929.4
1.817	2.126	7.215	107.8	28.51	5825.5	51.62	15453.6
1.916	2.203	8.249	179.3	29.32	6140.4	52.33	15551.2
2.025	2.572	9.354	282.0	30.61	6657.3	53.45	16230.7
2.121	2.906	10.37	404.3	31.43	7225.8	54.27	16497.6
2.214	3.199	11.02	496.1	32.72	7850.2	55.35	16802.3
2.345	3.705	11.94	644.6	33.84	7931.6	56.66	17548.5
2.429	4.018	12.95	828.8	34.65	8521.6	57.42	17742.4
2.510	4.392	13.79	1003.6	35.62	8725.9	58.40	18308.2
2.627	4.923	14.63	1199.7	37.45	9457.1	59.71	18766.4
2.728	5.480	15.82	1344.9	38.53	9909.4		

XII. APPENDIX D: HEAT CAPACITY OF ET-1 SAMPLE (NORMALLY d-hcp La) FROM 1 K TO 60 K, WHERE T IS IN KELVIN, C IN mJ/mole-K AND H IN OERSTED

H = 0		T	C	T	C	T	C
T	C	2.821	39.16	5.584	185.0	21.52	7462.5
		2.883	41.98	5.848	210.5	22.46	7919.6
1.005	1.199	2.966	45.94	5.933	217.5	23.27	8421.1
1.121	1.704	3.062	50.58	6.018	224.9	24.39	9101.8
1.213	2.238	3.151	55.33	6.082	224.8	25.32	9560.7
1.293	2.860	3.228	59.69	6.245	246.1	26.09	10129.9
1.379	3.605	3.302	63.76	6.403	266.4	27.04	10521.6
1.466	6.587	3.391	69.07	6.633	298.5	28.20	11197.8
1.545	5.326	3.475	74.54	6.856	340.1	29.51	11824.7
1.618	6.212	3.540	78.69	7.254	399.1	30.96	12503.4
1.694	7.296	3.623	84.20	7.775	507.3	32.55	13216.8
1.762	8.371	3.748	93.48	8.413	673.5	33.43	13587.8
1.850	9.724	3.833	100.1	9.027	831.8	34.44	13952.9
1.927	11.39	3.927	108.2	9.658	1042.7	35.21	14264.4
2.044	13.88	4.015	113.7	10.37	1311.9	36.51	14760.3
2.116	15.58	4.241	135.3	11.42	1744.1	37.97	15221.7
2.191	23.13	4.473	158.6	12.39	2207.8	38.71	15527.4
2.252	19.08	4.586	171.1	13.51	2731.9	39.46	15836.2
2.322	21.07	4.692	183.4	14.44	3184.6	40.58	16209.4
2.383	22.88	4.797	194.6	15.32	3597.4	41.65	16763.4
2.469	25.80	4.912	203.8	16.24	4213.3	42.43	16800.9
2.553	28.57	4.970	181.7	17.38	4807.2	43.61	17103.5
2.638	31.49	5.039	152.2	18.45	5551.4	44.20	17295.1
2.697	33.79	5.103	145.4	19.56	6110.7	45.53	17621.8
2.761	36.50	5.295	159.7	20.49	6759.3	46.85	18010.6

T	C	T	C	T	C	T	C
47.49	18164.6	1.077	11.04	2.216	27.52	4.811	116.2
48.32	18421.8	1.123	11.58	2.291	28.91	5.027	130.8
49.24	18652.2	1.208	12.59	2.347	29.93	5.245	147.2
50.71	19063.1	1.273	13.40	2.413	31.22	5.451	164.3
51.68	19319.4	1.303	13.77	2.486	32.74	5.694	187.1
52.54	19463.7	1.397	14.94	2.554	34.11	5.843	201.7
53.71	19677.1	1.435	15.44	2.592	34.95	6.032	221.0
54.66	19864.3	1.507	16.41	2.657	36.32	6.086	226.4
55.85	20038.9	1.565	17.20	2.755	38.49	6.128	231.9
56.62	20167.5	1.649	18.39	2.818	39.98	6.485	277.8
57.45	20301.4	1.723	19.48	3.015	44.68	6.904	339.5
58.53	20413.8	1.769	20.15	3.243	50.82	7.234	394.4
59.87	20621.9	1.822	20.95	3.472	57.74	7.517	449.9
		1.890	22.01	3.680	64.58		
H = 10 k		1.937	22.75	3.851	70.55		
		1.980	23.46	4.067	78.86		
T	C	2.062	24.81	4.264	87.24		
		2.100	25.22	4.459	96.40		
1.010	10.26	2.175	26.80	4.633	105.2		

XIII. APPENDIX E: HEAT CAPACITY OF ET-2 SAMPLE (d-hcp La) FROM 1 60 K, WHERE T IS IN KELVIN, C IN mJ/mole-K AND H IN OERSTED

H = 0		T	C	T	C	T	C
T	C	3.244	59.84	6.115	225.9	27.63	10811.7
		3.352	65.82	6.293	248.0	28.54	11302.3
1.001	1.134	3.439	71.47	6.483	271.7	29.59	11810.1
1.056	1.357	3.528	77.07	6.707	301.5	30.67	12400.7
1.123	1.680	3.620	83.03	6.966	339.2	31.45	12834.6
1.197	2.077	3.741	91.64	7.147	371.5	32.37	13152.6
1.252	2.458	3.873	101.6	7.821	498.1	33.43	13562.3
1.334	2.984	3.982	110.4	8.625	720.7	34.53	13972.0
1.408	3.579	4.037	114.9	9.174	862.8	35.48	14358.9
1.479	4.285	4.155	125.1	9.943	1124.3	36.39	14685.5
1.562	5.219	4.264	135.6	10.46	1240.3	37.46	15061.2
1.637	6.073	4.336	142.5	11.37	1681.4	38.53	15410.6
1.745	7.586	4.419	151.4	12.31	2107.2	39.62	15814.7
1.853	9.300	4.541	164.4	13.28	2608.6	40.34	16106.7
1.961	11.40	4.637	177.1	14.52	3145.5	41.25	16383.4
2.052	13.33	4.760	189.5	15.46	3681.5	42.33	16711.8
2.178	16.22	4.855	199.9	16.30	4173.0	43.47	17087.2
2.265	18.80	4.921	208.7	17.14	4580.8	44.41	17296.1
2.373	21.94	5.013	200.9	18.25	5301.9	45.38	17558.3
2.481	25.57	5.047	169.1	19.27	5929.1	46.60	17873.4
2.598	29.65	5.071	150.3	20.41	6610.4	47.57	18160.6
2.687	33.08	5.253	146.4	21.52	7318.1	48.66	18472.1
2.771	36.69	5.437	160.0	22.55	7904.5	49.45	18683.5
2.803	40.13	5.611	174.9	23.64	8543.7	50.37	18911.4
2.914	45.40	5.848	199.8	24.51	9127.3	51.53	19227.4
3.066	50.16	5.914	205.5	25.44	9562.2	52.47	19428.8
3.180	56.30	6.012	215.7	26.70	10329.0	53.67	19619.0

T	C
54.50	19760.3
55.44	19884.6
56.58	20103.7
57.61	20221.1
58.77	20398.9
59.94	20462.2

H = 5

T	C
4.512	159.8
4.539	166.3
4.580	169.0
4.627	176.1
4.684	181.4
4.746	196.9
4.776	192.6
4.804	196.3
4.835	200.0
4.853	203.1
4.882	206.3
4.927	209.0
4.963	212.1
5.053	160.2

H = 10

T	C
4.521	163.9
4.569	168.6
4.622	174.9
4.674	181.1
4.727	187.9
4.762	191.6
4.778	194.4
4.820	199.2
4.846	202.0
4.867	204.8
4.881	207.6
4.924	210.3
4.941	210.2
4.984	202.1
5.059	159.6

H = 500

T	C
1.308	1.487
1.559	3.685
1.739	6.266
1.842	8.042
2.021	11.40
2.133	13.76
2.308	18.85
2.493	24.16
2.702	31.18
2.883	38.20
3.010	44.61
3.151	51.68
3.265	57.37
3.377	64.40
3.564	75.66
3.719	85.61
3.860	95.81
3.996	106.7
4.102	113.2
4.174	118.1
4.278	129.5
4.446	138.8
4.461	144.5
4.511	150.9
4.586	164.3
4.599	141.7
4.662	119.8
4.802	118.2
4.867	120.4
4.894	121.9

H = 750

T	C
1.401	1.996
1.698	4.807
1.947	9.274
2.180	13.33
2.472	19.90
2.627	61.50
2.774	77.07
2.931	35.54
3.032	41.34
3.195	49.00
3.313	55.23
3.484	66.32
3.613	74.11
3.784	86.01
3.898	96.46
4.038	107.1
4.073	110.4
4.137	108.4
4.274	122.43
4.316	134.5
4.395	119.1
4.493	103.8
4.599	104.0
4.635	106.1
4.670	108.6

H = 1 k	
T	C
1.234	5.270
1.561	8.773
1.934	13.71
1.983	16.75
2.151	20.51
2.279	23.87
2.490	30.23
2.611	36.65
2.701	41.86
2.833	44.85
2.885	48.41
2.940	51.44
3.008	46.67
3.041	42.08
3.082	38.75
3.212	44.99
3.409	59.10
3.527	68.21
3.683	80.40
3.795	88.47
3.890	93.06
3.987	98.74
4.036	98.20
4.063	106.8
4.103	111.7
4.171	109.6
4.247	93.96

T	C
4.297	91.84
4.372	92.35
4.420	94.97
4.532	100.6
5.284	148.7
5.463	162.9
5.679	182.4
5.880	201.7
5.972	211.3
6.063	221.3
6.158	232.4
6.267	245.0
6.453	267.8
6.597	287.6

H = 1.25 k	
T	C
1.059	5.652
1.554	11.69
1.946	18.68
2.145	23.19
2.276	25.94
2.429	24.98
2.538	22.17
2.668	18.84
2.833	22.65
2.974	30.15

T	C
3.086	38.61
3.235	47.34
3.399	60.33
3.563	72.66
3.748	84.10
3.796	87.07
3.903	90.69
3.955	101.6
4.067	86.64
4.195	85.10
4.272	87.33
4.343	90.98

H = 1.5 k	
T	C
1.189	7.268
1.584	13.03
1.930	19.67
2.237	26.56
2.352	29.37
2.446	30.41
2.581	29.60
2.714	24.92
2.879	32.54
3.042	40.44
3.184	50.51
3.357	61.92

T	C
3.462	69.05
3.555	69.40
3.714	78.87
3.775	91.29
3.861	83.00
3.913	78.22
3.993	76.85
4.087	78.92
4.166	82.81

H = 3 k	
T	C
1.074	6.860
1.190	8.226
1.226	5.825
1.274	3.245
1.451	7.312
1.693	12.30
1.754	15.91
1.834	17.71
1.927	15.54
2.083	13.79
2.267	21.64
2.422	25.28
2.481	33.05
2.558	38.53
2.615	40.07

T	C
2.758	40.08
2.894	41.35
3.019	44.02
3.132	47.09
3.276	50.90

H = 10 k

T	C
1.005	10.07
1.091	11.06
1.174	12.01
1.245	12.87
1.304	13.61
1.379	14.54
1.428	15.17
1.493	16.02
1.549	16.76
1.606	17.56
1.656	18.24
1.738	19.44
1.803	20.39
1.864	21.36
1.944	22.57
2.005	23.58
2.042	24.20
2.133	25.75
2.184	26.62
2.256	27.85
2.328	29.22
2.392	30.45
2.470	31.98
2.526	33.12
2.596	34.58
2.636	35.46
2.726	37.40
2.825	39.63
2.902	41.45
2.955	42.75
3.003	44.00
3.126	46.99
3.255	50.44
3.368	53.73
3.431	55.60
3.512	58.11
3.637	62.20
3.763	66.75
3.880	70.81
3.974	74.21
4.035	76.68
4.139	81.03
4.253	85.88
4.348	90.21
4.472	96.34
4.539	99.99
4.661	106.4
4.756	111.8
4.818	116.5
4.962	125.1
5.039	130.9
5.125	136.8
5.243	145.3
5.301	149.5
5.482	164.1
5.554	170.8
5.647	179.1
5.738	187.8
5.840	198.0
5.951	209.3
6.047	219.5
6.139	229.7
6.238	241.3
6.356	255.6
6.405	261.6
6.573	284.0
6.728	305.4
6.982	350.0